

# Chemical exchange saturation transfer imaging and spectroscopy

Jinyuan Zhou <sup>a,b,\*</sup>, Peter C.M. van Zijl <sup>a,b</sup>

<sup>a</sup> Division of MR Research, Department of Radiology, Johns Hopkins University School of Medicine, 217 Traylor Building, 720 Rutland Avenue, Baltimore, MD 21205-2109, USA

<sup>b</sup> F.M. Kirby Research Center for Functional Brain Imaging, Kennedy Krieger Institute, 707 N. Broadway, Baltimore, MD 21205-1832, USA

Received 9 December 2005

Available online 18 April 2006

**Keywords:** Chemical exchange; Hydrogen exchange; Proton exchange; Exchange rate; Metabolite; Protein; Peptide; Amide proton; Lanthanide complex; Saturation transfer; Magnetization transfer; CEST (chemical exchange dependent saturation transfer); DIACEST (diamagnetic chemical exchange dependent saturation transfer); PARACEST (paramagnetic chemical exchange dependent saturation transfer); APT (amide proton transfer); Contrast agent; Contrast mechanism; pH imaging; Molecular imaging; MRI

## Contents

1. Introduction	110
2. Theory and background	111
2.1. Two-site exchange theory	111
2.1.1. Approximation of a weak saturation pulse and complete saturation	112
2.1.2. Steady-state solutions under the weak saturation pulse approximation	112
2.1.3. Time-dependent solutions under the weak saturation pulse approximation	113
2.2. Sensitivity enhancement mechanism	113
2.3. Chemical exchange dependent saturation transfer (CEST) and conventional magnetization transfer (MT)	114
3. Chemical exchange and pH dependence	115
3.1. Hydrogen exchange	116
3.2. Bound water exchange	118
4. Diamagnetic chemical exchange dependent saturation transfer (DIACEST)	119
4.1. Studies on small molecules	119
4.2. Macromolecular agents	120
4.3. DIACEST pH imaging	122
4.4. DIACEST reporter genes	123
5. Paramagnetic chemical exchange dependent saturation transfer (PARACEST)	124
5.1. PARACEST effects	124
5.2. PARACEST agents for pH reporting	125
5.3. Metabolite detection	126
5.4. PARACEST agents for cell labeling	127
5.5. Temperature measurement	128
6. Amide proton transfer (APT) imaging	128
6.1. In situ APT effects	128
6.2. pH Imaging using APT	129
6.3. APT imaging of brain tumors	131

\* Corresponding author. Address: Division of MR Research, Department of Radiology, Johns Hopkins University School of Medicine, 217 Traylor Building, 720 Rutland Avenue, Baltimore, MD 21205-2109, USA. Tel.: +1 410 955 7491; fax: +1 410 614 1948.

E-mail address: [jzhou@mri.jhu.edu](mailto:jzhou@mri.jhu.edu) (J. Zhou).

7.	Technical considerations	131
7.1.	Field strength and homogeneity	131
7.2.	Saturation scheme	133
7.3.	Interference from lipid signals	133
8.	Conclusions	134
	Acknowledgements	134
	References	134

## Nomenclature

2D	two-dimensional	MT	magnetization transfer
APT	amide proton transfer	MTR	magnetization transfer ratio
APTR	amide proton transfer ratio	PAA	polyallylamine
BOLD	blood-oxygen-level-dependent	PARACEST	paramagnetic chemical exchange dependent saturation transfer
CEST	chemical exchange dependent saturation transfer	PBS	phosphate buffer solution
cs	complete saturation	PCA	perchloric acid
CSF	cerebrospinal fluid	PEI	polyethylenimine
CW	continuous wave	PLE	poly-L-glutamate
DIACEST	diamagnetic chemical exchange dependent saturation transfer	PLL	poly-L-lysine
DOTA	1,4,7,10-tetraazacyclododecane-1,4,7,10-tetraacetate acid	Poly(rU)	polyuridilic acid
DOTMA	$\alpha, \alpha', \alpha'', \alpha'''$ -tetramethyl-1,4,7,10-tetraacetic acid	PTE	proton transfer enhancement
DTMA	1,4,7,10-tetraazacyclododecane tetrakis(methylacetamide)	PTR	proton transfer ratio
EPI	echo planar imaging	RF	radiofrequency
FSE	fast spin echo	s	solute exchangeable proton or solute-bound water proton pool
IEPA	2-imidazol-1-yl-3-ethoxycarbonyl-propionate	SNR	signal-to-noise ratio
LIPOCEST	CEST system using liposomes	SPD-5	generation-5 starburst PAMAM dendrimers
LRP	lysine rich protein	ss	steady-state
LW	line width	TR	repetition time
MAC	middle cerebral artery	w	bulk water proton pool
MACO	middle cerebral artery occlusion	WEX	water exchange

## 1. Introduction

The study of chemical exchange processes is one of the oldest and still most vigorously investigated topics in NMR spectroscopy. The effects of chemical exchange on the NMR spectrum were reported as early as 1951 [1,2] and investigated intensively during the early days of NMR [3–10]. In a landmark paper published in 1963, Forsen and Hoffman [8] studied moderately rapid chemical reactions by means of nuclear magnetic double resonance. Especially since the advent of two-dimensional (2D) NMR [11,12], numerous important advancements have occurred [13–16]. In addition to protons ( $^1\text{H}$ ), exchange spectroscopy has been applied to other NMR nuclei such as phosphorus ( $^{31}\text{P}$ ), fluorine ( $^{19}\text{F}$ ), and carbon ( $^{13}\text{C}$ ). Over the past half century, much valuable information on chemical reactions and exchange processes has been obtained by NMR spectroscopy studies. In the last six years, there has been a surge in NMR exchange applications because of the realization that saturation transfer experiments can be designed that allow a large sensitivity enhancement. The first to demonstrate that exchange between labile protons

of low-concentration solutes and water protons provides a sensitivity enhancement scheme were Balaban et al. [17–19], who dubbed this new MRI contrast mechanism chemical exchange dependent saturation transfer (CEST) [19]. After this initial work on small solutes, van Zijl and colleagues [20,21] showed that enormous increases in sensitivity could be obtained for macromolecules with a large number of exchanging sites of similar chemical shift. Enhancements as large as 500,000 were demonstrated for amide protons on cationic polymers [20], such as poly-L-lysine (PLL) and dendrimers, while a record enhancement of  $10^7$  or more was reported for the imino protons of polyuridilic acid (poly(rU)) [21]. At the same time, Zhang et al. [22,23] and Aime et al. [24] reported several paramagnetic CEST (PARACEST) agents that made the approach more flexible by significantly enlarging the frequency range for the exchanging sites. By analogy to this nomenclature, we will call the other compounds diamagnetic CEST (DIACEST) agents. In 2003, Zhou et al. [25,26] showed that endogenous mobile proteins and peptides at very low concentration in biological tissue could also be detected via the water signal. In this so-called amide proton transfer (APT)

imaging approach, the endogenous composite amide resonance around 8.3 ppm is saturated and detected indirectly by MRI, allowing the investigator to image tissue pH [25] and tissue protein and peptide content [26].

The large number of important achievements in NMR exchange spectroscopy since 1951 have been summarized in numerous excellent review articles [27–34] and textbooks [14,35–38] and are not covered in the current review. We also do not review exchange studies using heteronuclei such as  $^{31}\text{P}$  [15,16,39–47],  $^{19}\text{F}$  [48,49],  $^{13}\text{C}$  [50,51], and others. Instead, the goal of the current review is to present a systematic summary of proton saturation transfer studies in MRI and MRS with the purpose of imaging. Specifically, this review covers the first paper in this field suggesting the exchange enhancement in 1990 [17] and a number of important findings published between 1998 and November 2005. Because MRI is mostly a water-based approach in the clinic, we focus on water-related chemical exchange processes such as between low-concentration solute protons and water protons, which theoretically correspond to the case of exchange between a small pool being irradiated and a large pool being detected. The main reason that this approach is becoming important is that it presents a sensitivity enhancement scheme in which continuous saturation of the small pool causes cumulative saturation of the big pool, as will be explained below. Application of off-resonance irradiation saturation transfer is not the only way to image effects due to chemical exchange. Many alternative, non-saturation-transfer techniques have been proposed, including inversion transfer [52–55],  $T_1$  in the rotating frame [56–60],  $T_2$  in the rotating frame [61,62], and recently on-resonance exchange-sensitive low-power pulse trains [63], but these are not reviewed here. Finally, for more background reading, the early PARACEST findings including basic chemistry have been summarized in an excellent review article [64], and APT imaging has been reviewed in a recent conference proceeding [65].

An overview of exchange between small and large proton pools in principle would need to include both conventional magnetization transfer (MT) contrast [66–69] based on magnetization exchange between cellular solid and semisolid phases and the water protons, as well as the recent approach of CEST imaging, based on chemical exchange between protons of solutes and water. Conventional MT in biological tissues [66–69] has become a commonly employed MRI contrast parameter. Even though the exact mechanism is still under dispute, it is very likely that chemical exchange is a significant contributor [70–75] in addition to dipolar through-space magnetization exchange [66–69]. Many excellent reviews have appeared on classical MT imaging [67–69], and we here focus on the more novel approach of CEST imaging. CEST effects depend on several parameters, such as agent concentration, exchange rates, temperature, etc. In the brief period since 1998, researchers have suggested many different applications, including the design of new families of diamagnetic [20,21,76] and paramagnetic [22–24] MRI contrast agents, detection of metabolites [18,77–79], imaging of mobile proteins and peptides [26], and monitoring of pH

effects [19,24,25,80–83]. Even an MR reporter gene [84] based on the CEST principle has been designed. In view of the favorable property of CEST imaging contrast that it can be switched on-and-off at will, many more applications are expected in the future.

The present review consists of eight sections. Section 2 presents the theoretical background for CEST imaging and discusses its relationship to conventional MT contrast in vivo. Section 3 gives an overview of different types of exchangeable protons and their properties. Applications of CEST imaging and spectroscopy are summarized in Sections 4–6, respectively, corresponding to the three main members of the CEST family, namely, DIACEST, PARACEST, and APT. Section 7 deals with some technical issues that have to be kept in mind when using CEST technology.

## 2. Theory and background

### 2.1. Two-site exchange theory

The theoretical aspects of CEST generally aim at the description and quantification of the effects, and design and optimization of experimental schemes. For a spin system without scalar couplings, chemical exchange processes are commonly described by modified Bloch equations including exchange terms, sometimes called the Bloch–McConnell equations [6]. It is difficult to obtain the exact analytical solutions of these equations, even for the case of two-site exchange. Therefore, most investigators endeavor to derive concise analytical solutions of the problem using some reasonable assumptions. In addition, one is often interested in obtaining steady-state solutions or numerical solutions. For example, Zhou et al. [85] quantitatively described the case of two-pool exchange for CEST-type experiments by making several simplifying assumptions and approximations. When three or more different chemical environments are involved, a multiple-site exchange theory may be necessary, as discussed recently by Woessner et al. [86].

Similar to the previous work [85], Fig. 1 shows a sketch for the two exchanging pools, a small pool for endogenous or exogenous exchangeable solute protons or solute-bound water protons (s) and a large pool for bulk water protons (w). Parameters for MRI description of these pools and the exchange between them are also displayed. Defining  $\omega_0 = \gamma B_0$ ,  $\omega_1 = \gamma B_1$  (where  $\gamma$  is the nuclear gyromagnetic ratio,  $B_0$  the main magnetic field strength, and  $B_1$  the applied radio-frequency (RF) field strength),  $\Delta\omega = \omega - \omega_0$ , and assuming that the RF field is applied along the  $x$  direction in the rotating frame, the Bloch equations modified with exchange terms can be written as

$$\frac{dM_{xs}}{dt} = -\Delta\omega_s M_{ys} - R_{2s} M_{xs} - k_{sw} M_{xs} + k_{ws} M_{xw} \quad (1)$$

$$\frac{dM_{ys}}{dt} = \Delta\omega_s M_{xs} + \omega_1 M_{zs} - R_{2s} M_{ys} - k_{sw} M_{ys} + k_{ws} M_{yw} \quad (2)$$

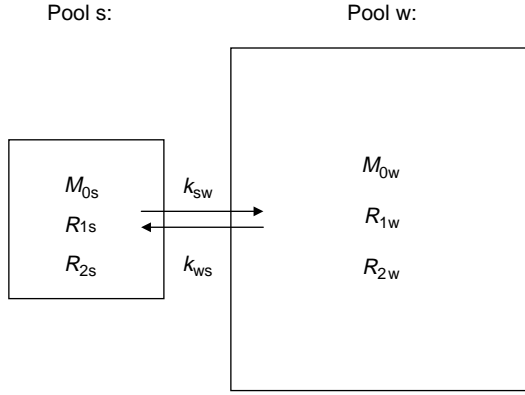


Fig. 1. Two-site chemical exchange model. The small pool (s) reflects dilute exchangeable solute protons. The large pool (w) reflects bulk water protons.  $R_1$ ,  $R_2$ , and  $M_0$  are the spin–lattice relaxation rate, spin–spin relaxation rate, and equilibrium magnetization, respectively.  $k_{sw}$  and  $k_{ws}$  are the exchange rates of protons from pool s to pool w, and vice versa. Reprinted from [85], with permission from Wiley-Liss, Inc.

$$\frac{dM_{zs}}{dt} = -\omega_1 M_{ys} - R_{1s}(M_{zs} - M_{0s}) - k_{sw}M_{zs} + k_{ws}M_{zw} \quad (3)$$

$$\frac{dM_{xw}}{dt} = -\Delta\omega_w M_{yw} - R_{2w}M_{xw} + k_{sw}M_{xs} - k_{ws}M_{xw} \quad (4)$$

$$\begin{aligned} \frac{dM_{yw}}{dt} = & \Delta\omega_w M_{xw} + \omega_1 M_{zw} - R_{2w}M_{yw} + k_{sw}M_{ys} \\ & - k_{ws}M_{yw} \end{aligned} \quad (5)$$

$$\frac{dM_{zw}}{dt} = -\omega_1 M_{yw} - R_{1w}(M_{zw} - M_{0w}) + k_{sw}M_{zs} - k_{ws}M_{zw} \quad (6)$$

in which  $R_1$  and  $R_2$  are the spin–lattice and spin–spin relaxation rates, respectively;  $M_0$  is the equilibrium magnetization;  $k_{sw}$  and  $k_{ws}$  are the exchange rates of protons from pool s to pool w and vice versa. The system under equilibrium obeys the relationship  $k_{sw}M_{0s} = k_{ws}M_{0w}$ . In contrast with a conventional MT imaging experiment, in which the two relevant pools (solid-like macromolecules and bulk water) can be treated as having identical chemical shifts (i.e. the same off-resonance terms) on the time scale of the MRI measurement and are distinguished only by relaxation parameters, the system we consider in this paper consists of two proton pools with different chemical shifts. This distinct resonance identity of the exchangeable solute protons is the prerequisite for successful application of CEST experiments. Thus, pool s does not include relatively abundant immobile macromolecular protons associated with conventional MT contrast, which resonate over a large spectral range of about 100–200 kHz. In addition, the transverse exchange terms need to be included in the equations, whereas these are often ignored in the description of conventional MT [87] in spite of a report of a possible contribution [88].

The number of differential equations can be reduced and some terms omitted under special assumptions. The most widely used approach is the weak saturation pulse

approximation [8,85], in which no direct water saturation occurs. The simplest solution of the equations is based on the assumption of complete saturation of irradiated protons [8,17–26]. It is important to mention several useful analytical solutions of the problem, including a solution of the strong saturation pulse approximation based on a double base transformation [89,90], a reasonable approximate solution suitable for an arbitrary RF saturation power [91] by combining the solution of the strong saturation pulse approximation with that of the weak saturation pulse case, and a comprehensive solution [92,93] in the presence of the effects of off-resonance irradiation, cross-relaxation, and chemical exchange.

### 2.1.1. Approximation of a weak saturation pulse and complete saturation

Assuming that the on-resonance RF field is applied to pool s (solute protons) with pool w (bulk water protons) unperturbed, we have  $\Delta\omega_s = 0$  and  $\Delta\omega_w \rightarrow \infty$ . Further assuming complete saturation (cs) of the irradiated protons, a simple solution can be obtained from Eq. (6):

$$M_{zw}^{cs} = \frac{R_{1w}}{R_{1w} + k_{ws}} M_{0w}. \quad (7)$$

Therefore, when pool s is completely saturated, the proton transfer ratio (PTR) for the water signal can be derived to be:

$$PTR^{cs} = \frac{M_{0w} - M_{zw}^{cs}}{M_{0w}} = \frac{k_{ws}}{R_{1w} + k_{ws}}. \quad (8)$$

Keep in mind that complete saturation can be obtained only under a very strong RF field, which is not a true case. As  $\Delta\omega$  and  $\omega_1$  terms are excluded in the expression, the solution cannot be used to quantify the spillover effects.

### 2.1.2. Steady-state solutions under the weak saturation pulse approximation

Similar to the previous work [85], we use the case-sensitive definitions:  $m_{zs} = M_{zs} - M_{0s}$ ,  $m_{zw} = M_{zw} - M_{0w}$ ,  $r_{1s} = R_{1s} + k_{sw}$ ,  $r_{1w} = R_{1w} + k_{ws}$ ,  $r_{2s} = R_{2s} + k_{sw}$ , and  $r_{2w} = R_{2w} + k_{ws}$ . If the RF field is applied to pool s only, the exchange-modified Bloch equations can be simplified to:

$$\frac{dM_{ys}}{dt} = \omega_1 m_{zs} - r_{2s}M_{ys} + k_{ws}M_{yw} + \omega_1 M_{0s} \quad (9)$$

$$\frac{dm_{zs}}{dt} = -\omega_1 M_{ys} - r_{1s}m_{zs} + k_{ws}m_{zw} \quad (10)$$

$$\frac{dM_{yw}}{dt} = -r_{2w}M_{yw} + k_{sw}M_{ys} \quad (11)$$

$$\frac{dm_{zw}}{dt} = -r_{1w}m_{zw} + k_{sw}m_{zs}. \quad (12)$$

The steady-state (ss) solutions of these four equations can be obtained exactly (namely, assuming that the left sides of the equations are all zero), and the results can be expressed as

$$m_{zs}^{ss} = -\frac{\omega_1^2 M_{0s}}{\omega_1^2 + pq} \quad \text{or} \quad M_{zs}^{ss} = \frac{pq M_{0s}}{\omega_1^2 + pq} \quad (13)$$

$$M_{ys}^{ss} = -\frac{\omega_1 q M_{0s}}{\omega_1^2 + pq} \quad (14)$$

$$m_{zw}^{ss} = -\frac{k_{sw}}{r_{1w}} \frac{\omega_1^2 M_{0s}}{(\omega_1^2 + pq)} = -\frac{k_{ws}}{r_{1w}} \frac{\omega_1^2 M_{0w}}{(\omega_1^2 + pq)} \quad (15)$$

$$M_{yw}^{ss} = -\frac{k_{sw}}{r_{2w}} \frac{\omega_1 q M_{0s}}{(\omega_1^2 + pq)} = -\frac{k_{ws}}{r_{2w}} \frac{\omega_1 q M_{0w}}{(\omega_1^2 + pq)} \quad (16)$$

in which  $p = r_{2s} - (k_{sw}k_{ws}/r_{2w})$  and  $q = r_{1s} - (k_{sw}k_{ws}/r_{1w})$ . For convenience, we define the labeling fraction or saturation efficiency for pool s:

$$\alpha = -m_{zs}^{ss}/M_{0s} = \omega_1^2/(\omega_1^2 + pq). \quad (17)$$

In particular, we should notice the difference between a steady state and a saturation state for pool s. Only when  $\omega_1 \rightarrow \infty$ , namely, under a very strong RF field, does pool s approach the saturation state,  $\alpha = 1$ . In most cases, the system never approaches true saturation, even though this term has been used widely for various MT experiments.

### 2.1.3. Time-dependent solutions under the weak saturation pulse approximation

The process of saturation transfer can approximately be separated into two steps, namely, the saturation or labeling process of pool s, followed by the transfer process of saturation to pool w. If pool s is completely isolated, its saturation rate can be estimated to be  $(R_{1s} + R_{2s})/2$ , meaning that pool s has a saturation time constant of tens of ms (in the order of  $T_{2s}$ ). Thus, this two-step approximation is very close to the actual situation. Assuming that pool s (exchangeable solute protons) approaches a steady state ( $m_{zs}^{ss} = M_{zs}^{ss} - M_{0s}$ ) instantly, the dynamics for pool w can be described by:

$$\frac{dm_{zw}}{dt} = -r_{1w}m_{zw} + k_{sw}m_{zs}^{ss}. \quad (18)$$

If  $M_{zw}(t_0) = M_{0w}$  (weak pulse approximation),  $m_{zw}(t_0) = 0$ . We have the solution:

$$m_{zw}(t) = \frac{k_{sw}m_{zs}^{ss}}{r_{1w}} [1 - e^{-r_{1w}(t-t_0)}]. \quad (19)$$

Thus, pool w approaches the steady state with a rate  $r_{1w}$  ( $=R_{1w} + k_{ws}$ ), which is the so-called spin-lattice relaxation rate of pool w (water protons) in the presence of RF irradiation on pool s (solute protons). This corresponds to a time constant in the order of  $T_{1w}$  ( $1 - 2s$ ) if  $k_{ws}$  is negligible. Therefore, the PTR in the water signal can be derived to be

$$\begin{aligned} \text{PTR} &= \frac{M_{0w} - M_{zw}(t_{\text{sat}})}{M_{0w}} \\ &= \frac{k_{sw}\alpha M_{0s}}{(R_{1w} + k_{ws})M_{0w}} [1 - e^{-(R_{1w} + k_{ws})t_{\text{sat}}}] \\ &= \frac{k_{ws}\alpha}{R_{1w} + k_{ws}} [1 - e^{-(R_{1w} + k_{ws})t_{\text{sat}}}] \end{aligned} \quad (20)$$

where  $t_{\text{sat}} = t - t_0$  is the applied RF saturation time.

The third equality of Eq. (20) is simpler, but the second may be more useful. The equations reflect that PTR depends on the exchangeable proton concentration of the solute and chemical exchange rate of the particular protons, as well as on saturation efficiency for pool s and  $T_1$  of the water ( $M_{0s} \propto [\text{solute proton}]$ ,  $M_{0w} \propto [\text{water proton}]$ ). Under in vivo conditions, PTR is also related to the water content of tissue ( $w$ ,  $[\text{water proton}] = 2 \times 55M \times w$ ). In addition, at fast exchange rates, high exchangeable proton concentrations, and a high magnetic field (low  $R_{1w}$ ),  $k_{ws}$  ( $k_{ws} = k_{sw}[\text{solute proton}]/[\text{water proton}]$ ) may become comparable with  $R_{1w}$ , and back exchange (water protons to solute protons) may be of influence.

### 2.2. Sensitivity enhancement mechanism

Using small molecules in solution (e.g. ammonia, urea), Balaban and his colleagues [17–19] demonstrated the possibility of CEST imaging in which RF saturation is transferred from exchangeable solute protons to water. Based on the transfer of magnetization between a small solute pool and a large water pool, a significant improvement in the signal-to-noise ratio for detection and imaging of the small pool can be obtained. Several promising research directions were proposed afterwards, including CEST on polymers [20,21], PARACEST [22–24] and in vivo APT [25,26]. The basic principle of the CEST enhancement is discussed in this subsection.

As described in Fig. 2, the small pool being irradiated (pool s) consists of the water-exchangeable protons of solutes (e.g. hydroxyl, amine, amide, or imino protons, etc.) while the large pool (pool w) consists of bulk water protons. Forward exchange ( $k_{sw}$ ) and back exchange ( $k_{ws}$ ) occur simultaneously between them. Low-concentration solute molecules are labeled by saturating their exchangeable protons with selective RF irradiation. Before saturation is applied, a small solute proton peak can generally be detected in the NMR spectrum, unless exchange is very fast on the NMR time scale. After saturating the solute exchangeable protons, saturation exchange with water protons takes place. If the water pool is much larger than the solute proton pool, saturated solute protons are replaced repeatedly by non-saturated water protons and accumulation of saturated protons in the water pool acts as a ‘saturation amplifier’. A few seconds of RF irradiation then leads to enhancement in sensitivity if the product of the exchange rate and saturation efficiency is sufficiently high (Eq. (20), the second term).



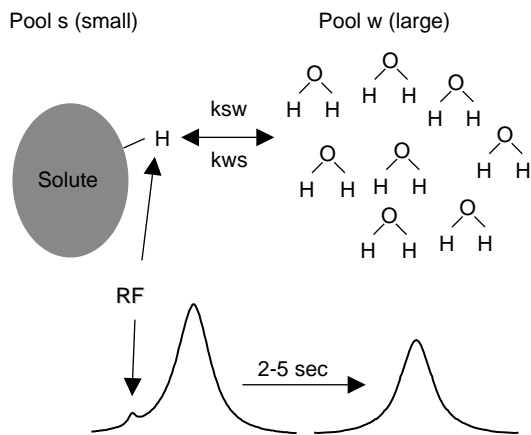


Fig. 2. CEST enhancement principle. Pool s reflects dilute exchangeable solute protons, and pool w reflects bulk water protons. Because a saturation RF field is applied to pool s, the small exchange proton peak disappears. During the application of the saturation field, saturated protons move to the large pool, while unsaturated ones move to the small pool. As a consequence, the water signal decreases significantly due to an accumulation of saturation transfer.

The proton transfer enhancement (PTE) can be derived directly from the PTR according to [20,21]

$$\text{PTE} = \frac{2[\text{H}_2\text{O}]\text{PTR}}{[\text{contrast agent}]}$$

$$= \frac{k_{\text{sw}}\alpha N_{\text{CA}}M_{\text{CA}}}{(R_{1\text{w}} + x_{\text{CA}}k_{\text{sw}})} [1 - e^{-(R_{1\text{w}} + k_{\text{ws}})t_{\text{sat}}}] \quad (21)$$

in which  $N_{\text{CA}}$  is the number of exchangeable protons per molecule applicable for the specific frequency irradiated,  $M_{\text{CA}}$  is the molecular weight, and  $x_{\text{CA}} = (M_{\text{os}}/M_{\text{ow}})$  is the exchangeable proton fraction. Notice that  $M_{\text{os}}$  is proportional to the exchangeable proton concentration, which is given by:

$$[\text{exchangeable proton}] = [\text{contrast agent}]N_{\text{CA}}M_{\text{CA}}. \quad (22)$$

If there are multiple exchangeable protons with multiple single-proton exchange rates resonating at the same frequency in the agent, PTE can be written as [20]:

$$\text{PTE} = \sum_i \frac{k_i\alpha_i N_i M_i}{(R_{1\text{w}} + x_{\text{CA}}k_i)} [1 - e^{-(R_{1\text{w}} + x_{\text{CA}}k_i)t_{\text{sat}}}] \quad (23)$$

To achieve the highest possible sensitivity enhancement, a large exchange rate  $k_{\text{sw}}$  and a high concentration of solute protons are needed at the particular irradiation frequency. The chemical exchange rate is a parameter of great physiological interest, because it depends on pH and the molecular environment, such as salt or metal content. When contrast agents are used, the limiting parameter is generally the agent concentration that can be achieved. For instance, in the pioneering studies of Balaban et al. [17–19] with small molecules and exchange rates on the order of a few 100 times per second, only concentrations of about 10–100 mM could be detected. Such detection sensitivities are still several orders of magnitude below those achievable with other contrast agents such as superparamagnetic tags and laser-polarized noble gases. When using DIACEST agents, exchange rates on the order of a few 1000 Hz are probably the limit for keeping

exchange slow on the NMR time scale. It is clear from Eq. (23) that the only other way to increase the effect appreciably is by increasing the number of exchangeable protons. Polymers therefore are a good type of CEST agents, and it was shown [20,21] that macromolecules with multiple amide groups or imino groups can give a CEST effect down to concentrations in the low micromolar range. On the other hand, as far as saturation schemes are concerned, we need enough saturation power and enough saturation time to be applied. A RF power level of a few  $\mu\text{T}$  is usually enough to be considered as complete saturation ( $\alpha=1$ ), and a labeling and saturation transfer period of a few seconds is enough for an efficient CEST experiment. Finally, a longer water  $T_1$  will increase the effect. Based on this and the higher frequency separation between solutes and solvents, the use of high magnetic fields is beneficial when using the CEST mechanism. A footnote here is that, when using short repetition times (TR), progressive saturation will reduce the CEST effects and that the interference of this effect is more disadvantageous at high field.

### 2.3. Chemical exchange dependent saturation transfer (CEST) and conventional magnetization transfer (MT)

Magnetization transfer is an extremely common physical phenomenon in NMR spectroscopy and imaging. Conventional MT measurements in vivo [66–69] have been based on the presence of a semi-solid macromolecular phase with a spectral width as large as 10 kHz that is approximately field strength-independent. When saturation is applied at a particular frequency far from the water resonance, this saturation is transferred rapidly between this solid-like matrix and free bulk water. Subsequently, there are two possible molecular mechanisms [72] responsible for MT. The first pathway is through dipolar coupling from protons of the immobilized macromolecular phase to protons of hydration water on the macromolecular surface to protons of the unbound bulk water. The second pathway is through the exchangeable protons of some side groups (e.g.  $-\text{OH}$ ,  $-\text{SH}$ , and  $-\text{NH}$ ), which mix with water protons via fast chemical exchange. The magnitude of MT is usually described by the so-called magnetization transfer ratio (MTR):  $\text{MTR} = 1 - S_{\text{sat}}/S_0$ , in which  $S_{\text{sat}}$  and  $S_0$  are the water signal intensities measured with and without RF saturation, respectively. In order to be in agreement with the original literature, this definition is sometimes equivalently written as another form:  $\text{MTR} = 1 - M_S/M_0$ . Notice the similarity with the CEST equations and that we have omitted the subscript w that stands for the large water pool.

In MT experiments, RF saturation effects on water are often displayed as a function of saturation frequency offset relative to water (Fig. 3), which is assigned to be at 0 ppm. This was originally referred to as an MT spectrum or a z-spectrum [68], or more recently as a CEST spectrum [19], in which the effect of saturation transfer at a specific irradiation frequency can be identified readily. It is important to compare the appearance of the z-spectrum from conventional MT with that for a typical CEST agent (Fig. 4). Conventional MT [66–69] can be detected over a very large frequency range, for example,

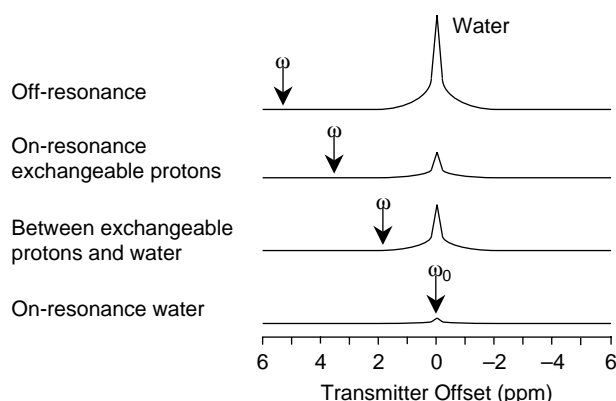


Fig. 3. Principle of z-spectroscopy or CEST-spectroscopy in which water saturation is measured as a function of irradiation frequency. When saturation RF pulses are applied at protons in magnetic contact with water, e.g. through chemical or dipolar exchange, the water signal has extra reduction. When irradiating close to the water resonance, direct saturation or ‘spillover’ occurs.

100 kHz. This frequency range is determined by the dipolar-dipolar interaction and chemical shift anisotropy for semi-solid macromolecules in tissue. CEST is usually detected in a small chemical shift range of less than 5 ppm from water for DIACEST, but could be as large as several 100s of parts per million for PARACEST agents. The main differences between MT and CEST are the frequency specificity of the CEST saturation effect and the approximately symmetric appearance of conventional MT with respect to the water resonance. Contrary to MT contrast, CEST effects originate from mobile molecules and depend purely on chemical exchange, while conventional MT depends on both chemical exchange and cross-relaxation.

It is not straightforward to demonstrate CEST effects on the water signal in tissues because of MT interference [66,67,69]. In addition, many CEST effects occur close to the water frequency and direct water saturation effects may interfere, especially at low magnetic fields. The effect of direct saturation is also called spillover [90,94,95]. Because the shape of the direct water saturation region of the z-spectra depends on  $T_{2w}$  and  $T_{1w}$ , changes in blood-oxygen-level-dependent (BOLD) effects [96–98] or water content will also influence the CEST spectrum [25,99]. To reduce the interference of these effects

with CEST measurements, it is useful to define an MT ratio asymmetry ( $MTR_{asym}$ ) parameter [18,25,26] by subtracting MT ratios obtained at the negative offset with respect to water from those at the corresponding positive offset:

$$MTR_{asym} = MTR(+offset) - MTR(-offset) \\ = S_{sat}/S_0(-offset) - S_{sat}/S_0(+offset). \quad (24)$$

If conventional MT effects were symmetric with respect to the water resonance, any contribution due to proton exchange should result in a positive MT difference. Unfortunately, however, the solid-like MT effect is somewhat asymmetric with respect to the water resonance, with a center frequency in the aliphatic range [100–102]. As a consequence, the resulting  $MTR_{asym}$  curve for offsets 0–5 ppm from water has an offset-dependent shape that depends on the inherent  $MTR'_{asym}$  of the solid-phase MT effect ( $MTR'_{asym}$ ) as well as on the PTR of the contributing exchangeable protons [25,26]:

$$MTR_{asym}(offset) = MTR'_{asym}(offset) + PTR(offset). \quad (25)$$

When comparing lesions or physiological alterations, PTR can be assessed under the assumption that  $MTR'_{asym}$  remains unaltered.

### 3. Chemical exchange and pH dependence

Chemical exchange is an extremely common phenomenon in the molecular world. Examples include internal rotation about a chemical bond, conformation flips, hydrogen exchange, substrate binding, etc. Because MRI in the clinic is mostly water based, the case of chemical exchange with water protons or chemical exchange of water molecules is particularly of interest for CEST imaging. The chemical exchange rates for several substances previously suggested for CEST imaging and the magnitude of the CEST effects measured under the particular experimental conditions are listed in Table 1. The requirements for a successful CEST experiment are that the exchangeable solute proton can be selectively and rapidly saturated, followed by rapid transfer to water and a long lifetime on the water to allow large enhancements. In terms of NMR, this means that one would like to have a high chemical exchange rate from the solute to

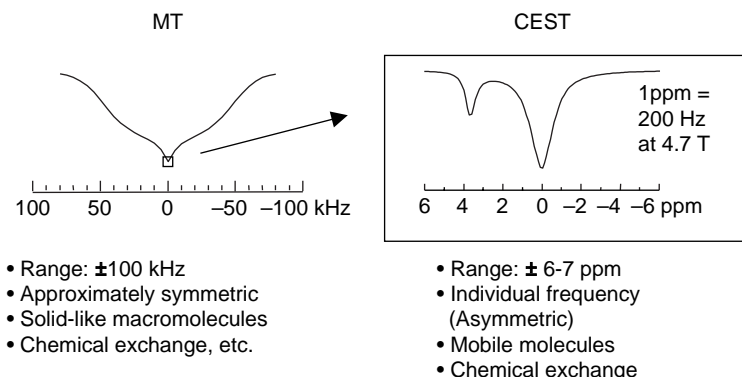


Fig. 4. Simulation of typical z-spectra for conventional MT and CEST. The CEST effect usually appears at a very narrow frequency range around the water resonance and is not taken into account in the common MT experiments.

Table 1  
Chemical exchange rates and the magnitude of CEST effects

Substance	Functional group	Chemical shift <sup>a</sup> (ppm)	Exchange rate (s <sup>−1</sup> )	$\Delta\omega_{\text{sw}}\tau_{\text{s}}$			CEST <sup>b</sup>
				11.7 T	4.7 T	1.5 T	
<i>Sugars</i>							
Mannitol	−OH	1.000	−	−	−	−	9.0% (7 T) [19]
Sorbitol	−OH	1.000	−	−	−	−	7.3% (7 T) [19]
Dextrose	−OH	1.500	−	−	−	−	8.7% (7 T) [19]
Lactose	−OH	1.333	−	−	−	−	20.9% (7 T) [19]
<i>Amino acids</i>							
L-Alanine	−NH <sub>2</sub>	3.000	−	−	−	−	67.4% (7 T) [19]
L-Arginine	−NH <sub>2</sub>	3.000	700 (pH 7.0, 36 °C) [72]	13.4	5.4	1.7	65.8% (7 T) [19]
L-Lysine	−NH <sub>2</sub>	3.000	4000 (pH 7.0, 36 °C) [72]	2.4	0.9	0.3	66.2% (7 T) [19]
L-Glutamine	−NH <sub>2</sub>	2.000	−	−	−	−	27.6% (7 T) [19]
<i>Others</i>							
5,6-Dihydrouracil	3−NH	5.000	−	−	−	−	22.2 (7 T) [19]
	2−NH	2.667	−	−	−	−	22.2 (7 T) [19]
Barbituric acid	−NH	5.000	−	−	−	−	32.5 (7 T) [19]
<i>Proteins and other polymers</i>							
Poly-L-Lysine	Amide protons	3.5	140 (pH 7.3–7.4, 37 °C) [20]	79	31	10	43% (11.7 T) [20]
Poly-L-Glutamate	Amide protons	3.5	10 (pH 7.3–7.4, 37 °C) [20]	1100	440	140	7% (11.7 T) [20]
Histone	Amide protons	3.5	39.6 (pH 7.05, 37 °C) [25]	278	111	35	20–30% (4.7 T) [25]
Dendrimer	Amide protons	3.5	77 (pH 7.3–7.4, 37 °C) [20]	143	57	18	51% (11.7 T) [20]
Poly(rU)	Imino protons	6.1	3080 (pH 7, 37 °C) [21]	6.2	2.5	0.8	13–72% (11.7 T) [21]
Rat brain tissue	Amide protons	3.5	28.6 (in vivo) [25] 10.1 (postmortem) [25]	384 1089	154 435	49 139	2.94% (4.7 T) [25] 1.04% (4.7 T) [25]
Rat 9L brain tumor	Amide protons	3.5	−	−	−	−	6.77% (4.7 T) [26]
<i>Lanthanide complexes</i>							
Pr-DOTA-4AmCE	Bound water	−60	50000 [23]	3.8	1.5	0.5	40% (4.7 T) [23]
Nd-DOTA-4AmCE	Bound water	−32	12500 [23]	8.0	3.2	1.0	48% (4.7 T) [23]
Eu-DOTA-4AmCE	Bound water	50	2618 [23]	60.0	24.0	7.7	57% (4.7 T) [23]
Yb-DOTA-4AmCE	Bound water	200	333333 [23]	1.9	0.8	0.2	No effect (4.7 T) [23]
Eu-DOTAM-Gly	Amide protons	−4	−	−	−	−	−
Dy-DOTAM-Gly	Amide protons	77	−	−	−	−	~2% (11.7 T) [24]
Ho-DOTAM-Gly	Amide protons	39	3448 [24]	35.5	14.2	4.5	~23% (11.7 T) [24]
Er-DOTAM-Gly	Amide protons	−22	3333 [24]	20.7	8.3	2.7	~30% (11.7 T) [24]
Tm-DOTAM-Gly	Amide protons	−51	2500 [24]	64.1	25.6	8.2	~40% (11.7 T) [24]
Yb-DOTAM-Gly	Amide protons	−16	2500 [24]	20.1	8.0	2.6	~68% (11.7 T) [24]

Adapted in part from [19], with permission from Academic Press, and in part from [23], with permission from Elsevier Science (USA).

<sup>a</sup> Relative to the resonance frequency of water.

<sup>b</sup> The effect of CEST depends on the solute concentration, pH value, temperature, field strength, saturation power, etc.; thus, the magnitude of CEST listed is approximate and for reference only.

the water ( $k_{sw}$ ), while maintaining the condition of slow exchange on the NMR time scale ( $\Delta\omega_{sw} \gg k_{sw}$  where  $\Delta\omega_{sw} = |\omega_s - \omega_w|$ ). Even though we will later see that this slow-exchange condition can be relaxed to intermediate exchange ( $\Delta\omega_{sw} \approx k_{sw}$ ), the choice of CEST agent will always be a balance between the need for a large chemical shift difference ( $\Delta\omega_{sw}$ ) and a large transfer speed. The use of higher magnetic fields favors this condition and, also in view of the increase of  $T_1$  values for water with field strength, CEST imaging is

therefore a true example of a method that benefits from higher magnetic field strength.

### 3.1. Hydrogen exchange

The organic molecules of the cell (sugars, amino acids, nucleotides, proteins, nucleic acids, etc.) contain several types of exchangeable protons, such as amine protons, S-bound, O-bound protons (exchange rates of several 100–



1000 Hz), and amide protons (exchange rate range of 1 to several 100 Hz). The rates of chemical exchange depend on the exchange types and environments. In general, the hydrogen exchange rates in aqueous solution can be described by [72,76,103–105]

$$k_{sw} = k_a[H^+] + k_b[OH^-] + k_0$$

$$= k_a \times 10^{-pH} + k_b \times 10^{pH-pK_w} + k_0 \quad (26)$$

in which  $k_a$ ,  $k_b$ , and  $k_0$  denote acid catalyzed exchange, base catalyzed exchange, and other possible contributions, respectively.  $OH^-$  and  $H_2O$  are potential base catalysts, and  $H_3O^+$  and  $H_2O$  are potential acid catalysts. There are many other catalysis mechanisms in pH buffers and biological tissue, but the above ones dominate.

Under physiological conditions (pH 7, 37 °C), the exchange rates of amines and S- and O-bound protons are generally too high for these protons to be detected by NMR because of severe line broadening and chemical shift averaging. The line widths (LW) of such resonances would be at least on the order of the exchange rate, namely,  $LW = (k + R_2)/\pi = 100\text{--}10,000$  Hz, which is much larger than the experimentally measured widths

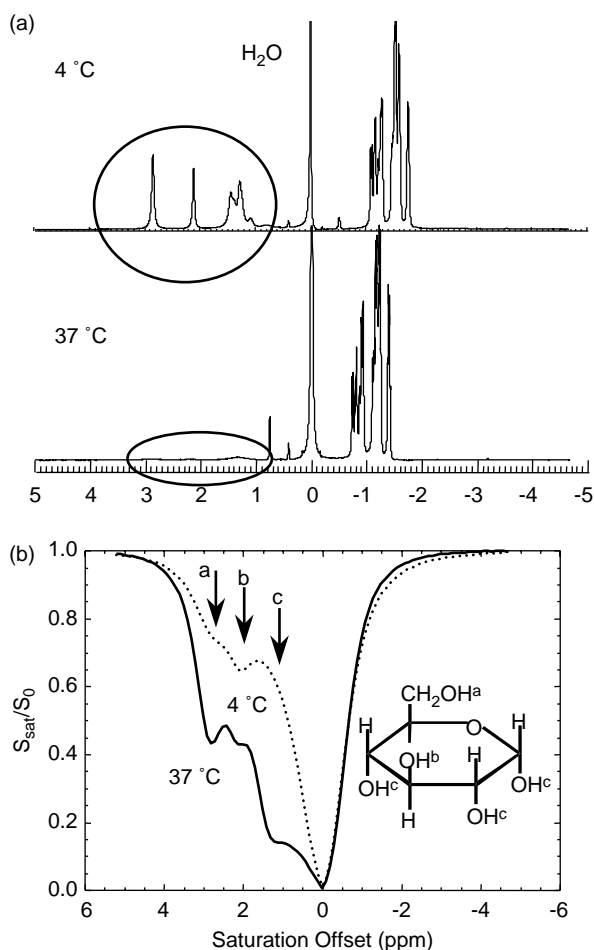


Fig. 5. 500 MHz  $^1H$  NMR spectra (a) and z-spectra (b) of  $\alpha$ -D glucose (300 mM, pH 3.5) at 4 and 37 °C. At higher temperature, the visibility of the rapidly exchanging hydroxyl protons reduces multi-fold in a standard NMR spectrum, while it increases in the z-spectrum.

of the peaks in the downfield spectral range in vivo. Interestingly, however, it is sometimes not impossible for such protons to be detected by CEST-MRI. The reason is that, contrary to NMR spectroscopy, where severe line broadening leads to a drastic lowering of signal-to-noise ratio (SNR), the CEST effect may still have similar or even higher sensitivity because at least partial saturation still occurs for most of the solute protons due to a finite irradiation bandwidth. This principle is illustrated in Fig. 5 for a glucose solution at low pH, where the NMR detectability reduces when going from low temperature (4 °C) to physiological temperature, while the CEST detectability approximately doubles.

Amide protons of peptides and proteins and imino protons of nucleic acids do have the appropriate exchange rate (Fig. 6, Table 1) to be detectable under physiological conditions. For example, as demonstrated by Snoussi et al. [21], polyuridylic acid (poly(rU)) is a sensitive CEST contrast agent due to two properties of the imino protons: a large rate of exchange with water protons and a sufficiently large difference in chemical shift from water protons to be detectable with CEST imaging. It was found [21] that the exchange rate of the poly(rU) imino protons with water is sensitive to pH and temperature. At pH 7 and 15 °C, the exchange rate constant is  $1213\text{ s}^{-1}$ . It increases to  $3080\text{ s}^{-1}$  at pH 7 and 37 °C, and to  $5880\text{ s}^{-1}$  at pH 7.3 and 37 °C. The pH dependence of the exchange rates of the imino protons of poly(rU) is characteristic of exchange catalyzed by  $OH^-$  (base-catalysis). Again, similar to the glucose example, Snoussi et al. [21] could not detect much signal in the proton spectrum of poly(rU) under physiological conditions, while enormous CEST effects were attained (order of  $10^7$  enhancement or more). Interestingly, when going from a concentration of 15–5  $\mu\text{M}$ , the CEST effect reduced only by about 20% instead of by a factor of three, indicating that back-exchange is still an issue even at these low concentrations. Extrapolating, it seems likely that the nanomolar range can be reached.

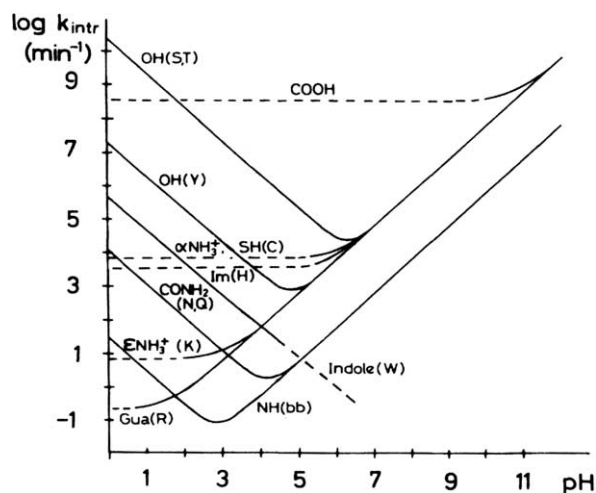


Fig. 6. Computed exchange rates for labile protons of polypeptides in  $H_2O$  solution at 25 °C as a function of pH. Im stands for imidazole ring NH, Gua for guanidinium NH, bb for backbone. Notice that the amide protons have a large range of possible exchange rates under physiological pH (pH 6.5–7.5). Reprinted from [104,105], with permission from Elsevier and Wiley, respectively.

Based on the *in vitro* results with large proteins, it seemed like a good idea to investigate possible endogenous CEST effects. However, even though proteins constitute about 18% of the total mass of a typical mammalian cell, only a fraction of these are sufficiently mobile to be MRS-detectable *in vivo*. Behar et al. [106–108] and Kauppinen et al. [109–111] first detected and identified several macromolecular peaks in brain proton MR spectra at low frequency (0–4 ppm). These signals were attributed to the aliphatic protons from mobile proteins, polypeptides, and lipids [106–115]. The backbone water-exchangeable amide protons of proteins [105], resonating in the 6–10 ppm range, are more difficult to detect because water suppression schemes may suppress signals of these protons due to exchange with saturated water protons. Using water-flip-back approaches and reduced saturation pulse sequences, Mori et al. [116] were able to observe a composite resonance around  $8.3 \pm 0.5$  ppm in the proton spectra of cancer cells and cat brain *in vivo*, which was assigned to these amide protons. Similar resonances were later found in rat brain [25,75] and human brain [117]. It was shown by Zhou et al. [25,26] that small CEST enhancements are detectable *in vivo*. These were dubbed APT effects to highlight their specific origin. It was estimated that the amide proton concentration (i.e. total amide protons over all proteins and peptides) was about 71.9 mM [25]. This gives a PTR of about 2.94% on the water line (3.2 M proton concentration), indicating that the CEST enhancement is about a factor of 45. The first human APT images were recently also reported by Jones et al. [118].

Similar to protein solutions, the exchange rates of endogenous amide protons in tissue have a strong pH dependence. Using water exchange (WEX) spectroscopy [119,120], Zhou et al. [25,75] investigated the amide proton exchange rates and the amide proton signal intensities *in situ* in the rat brain just before and just after cardiac arrest. It was determined (Fig. 7) that the amide proton content remains constant in this early postmortem period, while the amide proton exchange rate changes from  $28.6 \pm 7.4 \text{ s}^{-1}$  *in vivo* to  $10.1 \pm 2.6 \text{ s}^{-1}$  postmortem. Because of the lack of change in amide intensity, it was concluded that this rate change is due to the pH reduction upon death. To calibrate the exchange rate changes in terms of intracellular pH ( $\text{pH}_i$ ) changes, phosphorus spectroscopy was also performed, giving  $\text{pH}_i$  values of  $7.11 \pm 0.13$  and  $6.66 \pm 0.10$  for *in vivo* and postmortem, respectively. Using the fact that amide proton exchange is predominantly base-catalyzed [72,76,103–105] for  $\text{pH} > 5$ , the following equations were deduced

$$k_{\text{sw}} = k_{\text{b}}[\text{OH}] = k_{\text{b}} \times 10^{\text{pH} - \text{p}K_{\text{w}}} = 5.57 \times 10^{\text{pH} - 6.4} \quad (27)$$

in which  $\text{p}K_{\text{w}} = 15.4$  at  $37^\circ\text{C}$  [121].

### 3.2. Bound water exchange

Chelates of paramagnetic ions, such as gadolinium–DTPA used for clinical diagnosis, shorten bulk water proton longitudinal relaxation times through rapid exchange of an inner-sphere bound water molecule with bulk water [122–129].

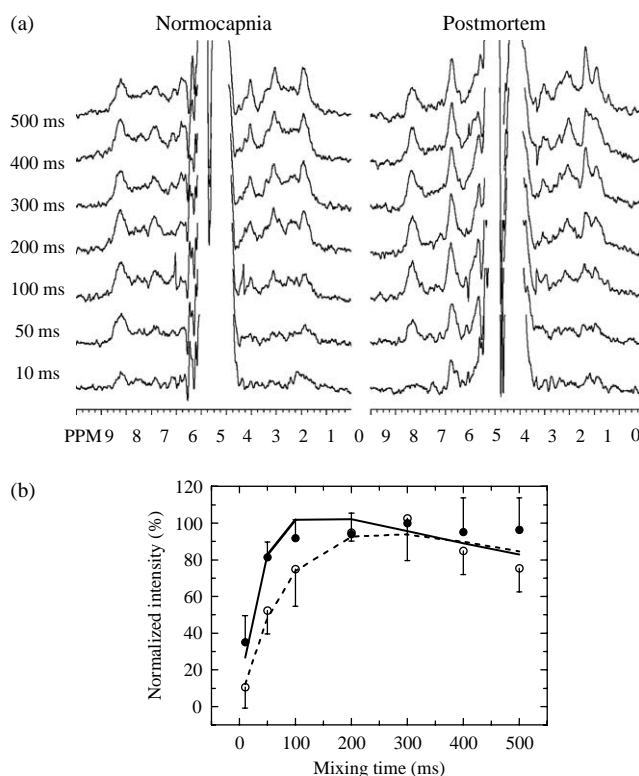


Fig. 7. (a) *In situ* water exchange (WEX) 4.7 T  $^1\text{H}$  spectra for rat brain as a function of mixing time between water inversion and spectral detection. Volume  $16 \times 12 \times 4 \text{ mm}^3$ , SW 3000 Hz, 1024 points, 256 scans, TR 4 s, and TE 8 ms; (b) fitting of proton exchange rates using the average amide proton integrals at 8.3 ppm ( $n=5$ ) as a function of mixing time. Integrals were normalized to the normocapnic value at  $t_m=300$  ms. Reprinted from [25], with permission from the authors and Nature Publishing Group.

As a result, the bound and bulk water NMR signals usually overlap and cannot be detected separately or irradiated separately. However, this is not always the case. Aime et al. [130] reported that the  $^1\text{H}$  NMR signal of bound water was detectable in  $\text{EuDTMA}^{3+}$  (where DTMA = 1,4,7,10-tetraazacyclododecane tetrakis(methylacetamide)) at low temperatures in acetonitrile- $d_3$ . Three years later, Zhang et al. [131] showed that a variety of DOTA-tetra(amide) complexes (where DOTA = 1,4,7,10-tetraazacyclododecane-1,4,7,10-tetraacetate acid, see Fig. 8) also have sufficiently slow bound water exchange kinetics (Table 1). In this study, the chemical shifts of the  $\text{Ln}^{3+}$ -bound water protons were observed or estimated to be from  $-720$  to  $500$  ppm (relative to the bulk water) at  $25^\circ\text{C}$ . The bound water lifetime ( $\tau_s = 1/k_{\text{sw}}$ ) was estimated to be from  $\mu\text{s}$  to  $\text{ms}$ , depending on the extended pendent arms in these derivatives. This lifetime is sufficiently long to observe a

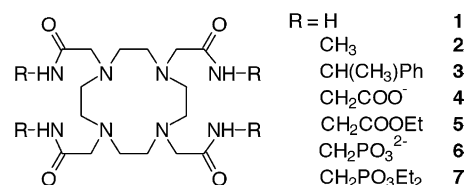


Fig. 8. Structure of DOTA-tetra(amide) ligands. Reprinted from [23], with permission from Elsevier Science (USA).

$\text{Ln}^{3+}$ -bound water signal in both the  $^1\text{H}$  and  $^{17}\text{O}$  NMR spectra in aqueous solution at ambient temperatures, and therefore for these paramagnetic compounds to function as CEST agents. Aime et al. [24] explored another series of lanthanide(III) complexes ( $\text{Ln}=\text{Eu}$ ,  $\text{Dy}$ ,  $\text{Ho}$ ,  $\text{Er}$ ,  $\text{Tm}$ ,  $\text{Yb}$ ) with the macrocyclic DOTAM-Gly ligand (Table 1), a tetraglycineamide derivative of DOTA. These complexes display two types of exchange, namely, coordinated water and amide proton exchange. In these chelates, the chemical shifts of the amide protons are distributed from  $-51$  to  $77$  ppm, while the signal of the coordinated water was not detectable in the proton NMR spectra at room temperature and  $7.05$  T, probably due to its faster exchange rate.

#### 4. Diamagnetic chemical exchange dependent saturation transfer (DIACEST)

##### 4.1. Studies on small molecules

Wolff and Balaban [17] were the first to image the spatial distribution of proton chemical exchange effects in solution phantoms. In their pioneering work, they studied proton exchange between ammonium chloride and water at  $4.7$  T and demonstrated that saturation transfer can be used as a sensitivity enhancement scheme. When studying a  $62.5$  mM solution of  $\text{NH}_4\text{Cl}$ , they observed that only the water resonance could be detected in the NMR spectrum, while the ammonium proton signal ( $\sim 2.5$  ppm =  $500$  Hz from water) was invisible. However, when irradiating at the ammonium proton frequency, they detected a  $50\%$  decrease in the water signal intensity. In other words, NMR sensitivity was enhanced from  $62.5$  mM to  $55$  M (or  $880$ -fold). Fig. 9 shows proton images of a dual-compartment phantom with  $\text{NH}_4\text{Cl}$  solution in the outer part. When applying RF irradiation at the offset of  $500$  Hz, the signal in the outer region decreased strongly with respect to that in the central pure water area, thus producing chemical exchange dependent MRI contrast. The new class of agents that can produce such contrast were dubbed CEST agents.

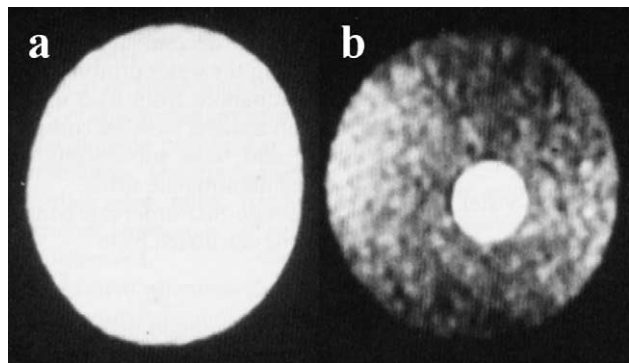


Fig. 9. First demonstration of CEST imaging by Wolff and Balaban. The inner part contains pure water, and the outer contains a dilute ammonium chloride solution ( $25$  mM,  $\text{pH} \sim 5.4$ ). RF irradiation was applied at  $-2.5$  (a) and  $+2.5$  ppm (b) from the water resonance, showing the transfer effect of the saturated ammonium protons. Modified (a and b inverted) from [17], with permission from Academic Press.

The use of saturation transfer for the measurement and imaging of proton chemical exchange between metabolites and water in biological tissues *ex vivo* was first explored by Guivel-Scharen et al. [18], who conducted MT experiments on a variety of samples, including the rat brain, muscle, spleen, heart, and liver, as well as the cortex and medulla of the rabbit kidney. Such experiments present a whole new set of experimental problems. First of all, unlike solutions, biological tissues have  $z$ -spectra that are dominated by large conventional MT effects associated with the interaction between semi-solid macromolecules and bulk water. Moreover, the effects of direct water saturation increase due to the short  $T_2$  in tissue. Consequently, as described above, it is necessary to perform an asymmetry analysis [18,25,26] in an effort to separate out the pure proton chemical exchange from other concomitant effects. When studying the above biological tissues, Guivel-Scharen et al. found that the rabbit kidney medulla shows the largest asymmetry in the MT spectra, with maximum effects at  $\sim 2.6$  and  $\sim 1$  ppm from water (Fig. 10a). To reveal the source of this effect, they performed several extra experiments. They found that both perchloric acid (PCA) extracts, in which the denatured proteins and structural elements are removed, and urine, which contains many of the metabolites found in the kidney medulla, show an MTR asymmetry similar to that detected in the intact medulla (Fig. 10). They therefore attributed this MTR asymmetry in the rabbit medulla to low-molecular-weight nitrogen-containing metabolites such as urea and ammonia. In follow-up experiments on a  $500$  MHz microimaging system, Guivel-Scharen et al. [18] used MRI to confirm the large and specific MTR asymmetry in the intact kidney *ex vivo*. In their experiment, the off-resonance RF irradiation was applied at offsets of  $\pm 1.74$  ppm from water, corresponding to the center of the large asymmetry range in the  $z$ -spectrum and a symmetry reference. As seen in Fig. 11, there is a CEST effect in the medulla. Further analysis showed that the effect in the medulla increased linearly from the cortico-medullary region to the papillary tip. In an ultimate effort, Dagher et al. [77] tested the feasibility of *in vivo* CEST imaging of urea for five normal volunteers. The results show that chemical exchange is indeed detectable in the kidney at the offset of approximately  $100$  Hz in a standard  $1.5$  T clinical scanner.

When designing new CEST contrast agents, it is important to evaluate which substances or chemical exchange sites could function effectively under physiological conditions. Toward this goal, Ward et al. [19] evaluated the CEST properties of numerous exchangeable groups in sugars, amino acids, and many other compounds. Table 1 lists part of the findings reported in their work. It was shown that the magnitude of CEST depends on exchange site concentration, pH, phosphate concentration, temperature, and some other factors [19]. They also noticed that polymerization provides a method to increase the number of exchange sites per mole. Fig. 12 shows some typical examples. Based on their results, several conclusions could be drawn. (i) The CEST process strongly depends on pH and temperature. For some agents it could be possible that the exchange moves from slow to intermediate exchange range when changing one pH unit or  $10^\circ\text{C}$ . (ii) Compounds can possess multiple exchange sites



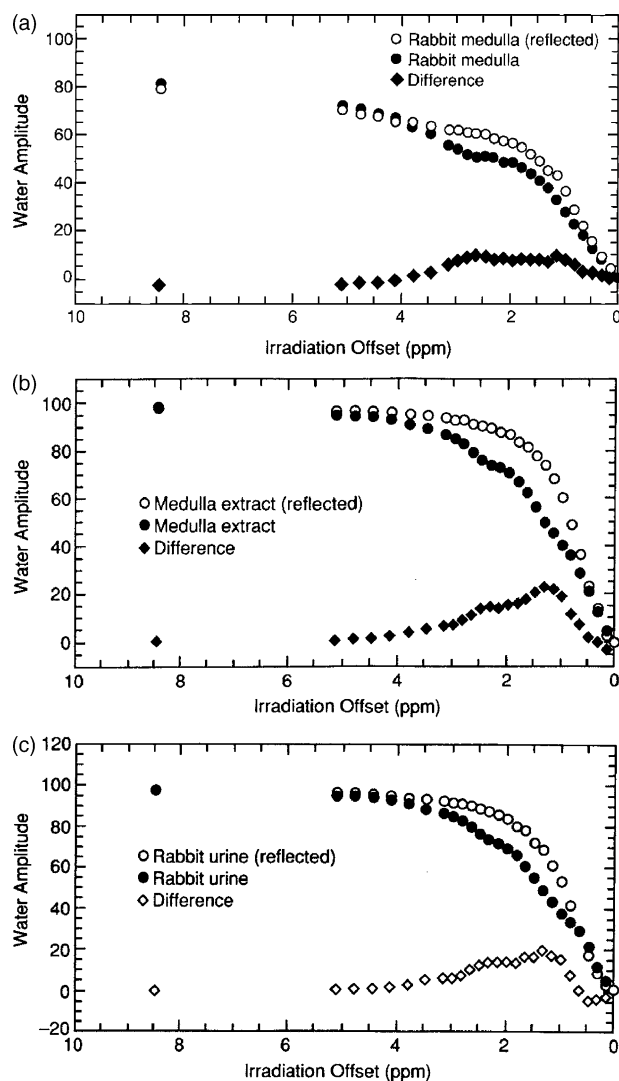


Fig. 10. z-Spectra for high-frequency (positive offset with respect to water offset) and low-frequency (negative offset with respect to water, denoted as 'reflected') irradiation, together with  $MTR_{\text{asym}}$  spectra (denoted as 'difference'). (a) Rabbit kidney medulla, (b) perchloric acid extract of a rabbit kidney medulla, and (c) rabbit urine at pH 7.8. Reprinted from [18], with permission from Academic Press.

with different CEST properties. (iii) When entering the intermediate exchange range, the CEST spectrum is broadened and the CEST peak shifts toward the water resonance. (iv) The effect of phosphate on the CEST spectra can differ between different exchange sites present on the same molecule. (v) The CEST effect linearly increases with [agent], but the lineshape of CEST is maintained. Although these effects seem very complicated, they can mostly be explained using the theory in Section 2 and basic knowledge about proton exchange in the literature, especially based on the effect of proton accessibility in base- and acid-catalyzed exchange.

#### 4.2. Macromolecular agents

A polymer can possess multiple functional groups. When these contain exchangeable protons with the same chemical

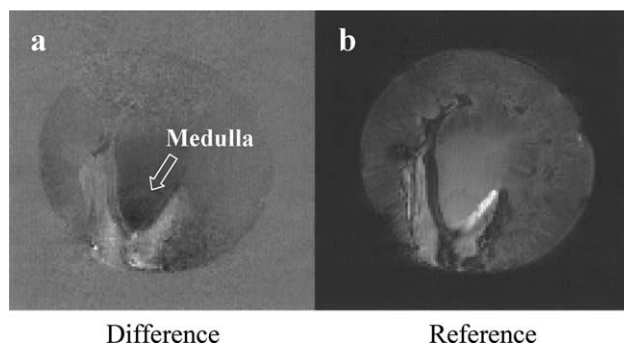


Fig. 11. CEST imaging of the rabbit kidney ex vivo at 500 MHz. Different from Fig. 10, the difference image was obtained from the experimental irradiation at 1.74 ppm minus the reference irradiation at  $-1.74$  ppm. A decrease in signal intensity, such as seen in the medulla, thus corresponds to regions with chemical exchange saturation transfer. The more the decrease, the stronger the CEST effect. Images were collected with a gradient recalled echo sequence. RF power was  $1.5 \mu\text{T}$ . The irradiation at  $-1.74$  ppm was called 'reference', while a scan in the absence of RF irradiation was called 'control' in this review. Modified from [18], with permission from Academic Press.

shifts they function as a CEST agent with high exchangeable site concentration. Exploiting the inherent properties of polymer amide protons that rapidly exchange with water, Goffeney et al. [20] showed that enhancements in sensitivity by factors as large as 500,000 are possible for amide protons on cationic polymers. Such polymers have recently gained importance as non-viral DNA delivery systems for potential use in gene therapy. From the viewpoint of in vivo CEST measurements, amide hydrogen exchange has a favorable exchange rate range ( $\sim 10\text{--}1000 \text{ s}^{-1}$ ) under physiological conditions. On the other hand, amine protons have a very high exchange rate. Therefore, several amide and amine containing compounds were evaluated, including PLL, poly-L-glutamate (PLE), generation-5 starburst PAMAM dendrimers (SPD-5), polyallylamine (PAA), and polyethylenimine (PEI) (see Fig. 13). CEST effects were detected for PLL, PLE, and SPD-5, but not for PAA and PEI, confirming that the feature of exchanging sufficiently slow on the NMR time scale to allow selective irradiation is a principal requirement for the present approach. Thus, for PAA and PEI, a single resonance coinciding with water occurs, and targeted detection is not possible. The measured enhancements for the amide protons can be predicted well using simple theory and experimental exchange rates measured using water exchange spectroscopy. Samples were prepared using approximately equal  $x_{\text{CA}}$  for PLL and SPD-5 (0.00211 and 0.00229, respectively), but despite the appreciable exchange rate difference ( $\sim 140$  vs.  $\sim 77 \text{ s}^{-1}$ ) approximately equal CEST effects (43 and 51%) were measured. This can be partially explained through the occurrence of back-exchange in PLL, but even when this is included, the theoretically predicted and measured effects are different (theory: 53 and 40%). The reduced effect in PLL was attributed to a failure of the assumption of complete saturation, while the SPD-5 deviation was discussed in light of the difficulty of determining the exchange rate properly as there are three different amide groups that partially overlap in chemical shift, each of which has a different exchange rate.

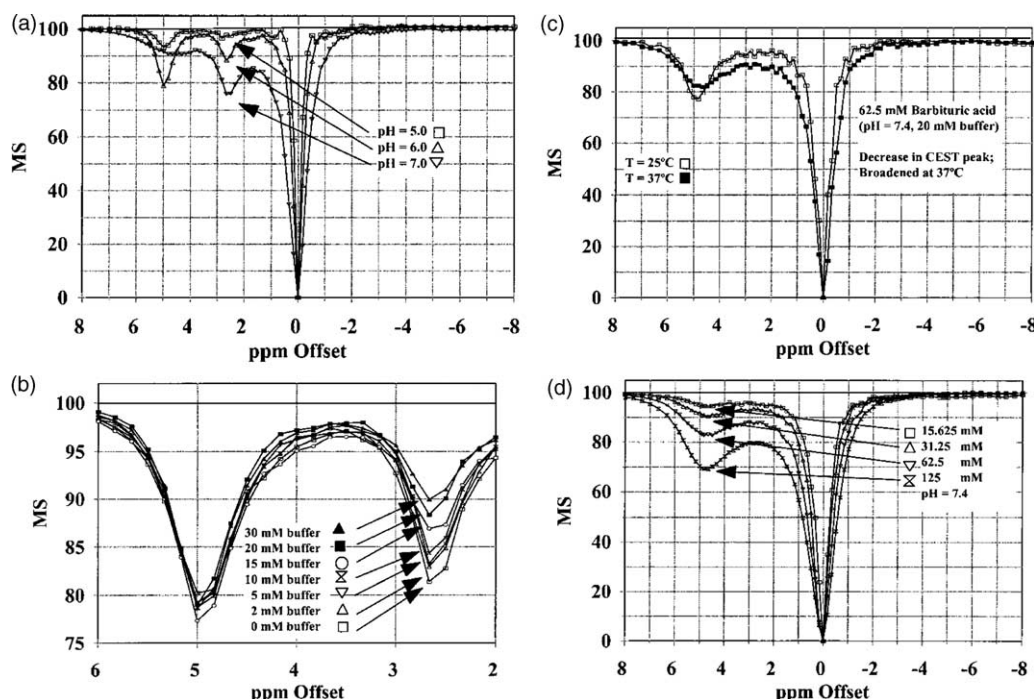


Fig. 12. (a) pH-dependent CEST spectra of 5,6-dihydrouracil (62.5 mM, 37 °C, 20 mM phosphate buffer). Exchange sites are visible at 5.00 and 2.67 ppm. (b) CEST spectra of 5,6-dihydrouracil solutions with varying levels of phosphate buffer (62.5 mM, 37 °C, pH 6.0). (c) Temperature-dependent CEST spectra of a barbituric acid solution (62.5 mM, 20 mM phosphate buffer, pH 7.4). (d) CEST spectra of barbituric acid solutions as a function of concentration (37 °C, 20 mM phosphate buffer, pH 7.0). All spectra were recorded at 7 T. Reprinted from [19], with permission from Academic Press.

Snoussi et al. [21] demonstrated that the exchange properties of the imino and hydroxyl protons of poly(rU) are in the appropriate range for use as a CEST contrast agent. Despite the strong line broadening due to the large imino proton exchange rate ( $\sim 5880 \text{ s}^{-1}$ ) at pH 7.3 and 37 °C, the chemical shift difference with water (10.8 vs. 4.8 ppm) is large enough to allow irradiation of the poly(rU) imino protons. When using low powers (0.1 mW), hydroxyl proton saturation at 6.4 ppm could even be detected, which became more difficult at higher power levels due to direct water saturation. The authors discussed the importance of different definitions for proton transfer enhancement. For instance, in the original definition (Eqs. (21)–(23)), the enhancement increases when more units are added to a polymer, while the enhancement would be the same from the more physical point of view of on a per proton basis. Under the conditions of long saturation time, complete saturation ( $\alpha = 1$ ), and sufficiently low contrast agent concentration to avoid back exchange, they provided three definitions for maximal signal enhancement:

$$\text{PTE}_{\text{max}} = N_{\text{CA}} M_{\text{CA}} k / R_{1w} \quad (\text{per molecule basis}) \quad (28)$$

$$\text{PTE} / (N M_{\text{CA}})_{\text{max}} = k / R_{1w} \quad (\text{per proton basis}) \quad (29)$$

$$\text{PTE}(m)_{\text{max}} = N_{\text{CA}} k / R_{1w} \quad (\text{per molecular weight basis}). \quad (30)$$

Table 2 compares these measured enhancements as calculated from the experimental CEST effect using  $\text{PTE} = \text{PTR} / x_{\text{CA}} = (1 - S/S_0) / x_{\text{CA}}$ . The largest proton-transfer enhancement for this poly(rU) of 644 kDa was measured to be  $10^7$ , about 20 times higher than the value measured previously

for a poly(L-lysine) of 488 kDa [20]. When studying the table, the effect of back-transfer of saturated water protons is obvious, as shown by the fact that an increase in the contrast agent concentration by three times (5–15  $\mu\text{M}$ ) at the same power level (1 mW) increases the CEST effect factor by only

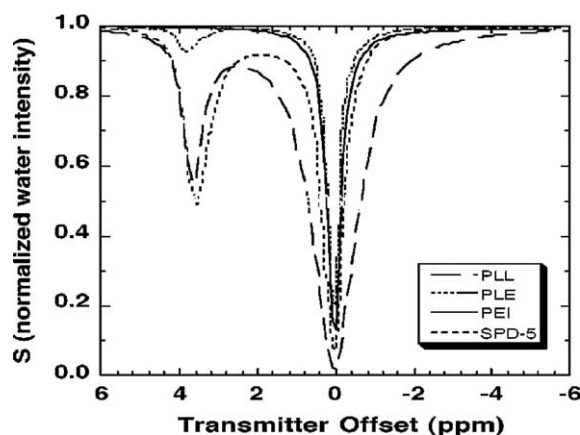


Fig. 13.  $^1\text{H}$  z-spectra for cationic polymers obtained at 500 MHz,  $T = 37^\circ\text{C}$ , and pH 7.3–7.4. CEST effects of different magnitude were measured for solutions of approximately equal amide proton concentration ( $x_{\text{CA}} = 0.0021$ – $0.0029$ ) for PLL (100  $\mu\text{M}$ ,  $N_{\text{CA}} = 4.78$  protons/kDa,  $M_{\text{CA}} = 488$  kDa), PLE (500  $\mu\text{M}$ ,  $N_{\text{CA}} = 6.62$  protons/kDa,  $M_{\text{CA}} = 70$  kDa), and SPD-5 (1000  $\mu\text{M}$ ,  $N_{\text{CA}} = 8.74$  protons/kDa,  $M_{\text{CA}} = 28.825$  kDa). Potential agents with amine protons were also tested: PAA ( $x_{\text{CA}} = 0.0041$ , 300  $\mu\text{M}$ ,  $N_{\text{CA}} = 21.61$  protons/kDa,  $M_{\text{CA}} = 70$  kDa) and PEI ( $x_{\text{CA}} = 0.0095$ , 150  $\mu\text{M}$ ,  $N_{\text{CA}} = 9.29$  protons/kDa,  $M_{\text{CA}} = 750$  kDa). The curves for PAA and PEI coincided and only the one for PEI was displayed. No noticeable effect was found for PAA and PEI. Reprinted from [20], with permission from American Chemical Society.



Table 2

Proton transfer enhancement factor (PTE) for the imino protons of poly(rU) and for the amide protons of the dendrimer ( $G=5$ )

Contrast agent <sup>a</sup>	Concentration ( $\mu\text{M}$ )	Power (mW)	$(1 - S_{\text{sat}}/S_0)$	(PTE/1000) <sup>b</sup>	PTE/(NM <sub>CA</sub> ) <sup>c</sup>	PTE(m) <sup>d</sup>
1. Poly(rU)	15	0.1	0.125	920	460	1.43
2. Poly(rU)	15	0.3	0.395	2900	1450	4.50
3. Poly(rU)	15	1.0	0.630	4620	2310	7.17
4. Poly(rU)	15	3.0	0.715	5240	2620	8.14
5. Poly(rU)	5	1.0	0.490	10800	5400	16.77
6 Dendrimer–poly(rU) <sup>e</sup>	10 <sup>f</sup>	1.0	0.420	4620	2310	4.95
7 Dendrimer <sup>g</sup>	100	1.0	0.150	165	82	5.68

Reprinted from [21], with permission from Wiley-Liss, Inc.

<sup>a</sup> Poly(rU) is a polymer of 2000 uridine units, 644 kDa. In the dendrimer–poly(rU) complex, one poly(rU) is associated to 10 dendrimers (29 kDa each) of 250 subunits, for a total mass of 933 kDa.<sup>b</sup> As per Eq. (21).<sup>c</sup> This is the proton-for-proton sensitivity enhancement.<sup>d</sup> As per Eq. (30). The mass per proton is 322 Da for poly(rU) and 14.5 Da for the dendrimer.<sup>e</sup> Irradiation at the frequency of the imino proton of poly(rU).<sup>f</sup> 10  $\mu\text{M}$  of complex includes 10 and 100  $\mu\text{M}$  of poly(rU) and dendrimer, respectively.<sup>g</sup> Irradiation at the frequency of the amide proton of the dendrimer.

about 20–30%. Based on this, the authors concluded that the enhancement factor would increase further at even lower concentrations of the contrast agent. For example, for a poly(rU) concentration of 0.5  $\mu\text{M}$ , the water signal attenuation can be estimated to be 19% [21], indicating that the nanomolar range is within reach of NMR detection.

In addition to studying the RNA polymer, the authors showed that the imino proton exchange properties could still be exploited when binding poly(rU) to a dendrimer gene carrier. This stoichiometric dendrimer–poly(rU) complex (about 10 dendrimers per poly(rU) unit) is expected to be able to cross the anionic cell membrane barrier. Fig. 14 compares the z-spectra for the complex and for the individual compounds. On a per proton basis, the CEST effect for the complex was found to be about 20% of that of the poly(rU) unit, when calculated back to the same concentration per construct. This is still very reasonable and, in view of the positive charge, it was concluded that this complex may provide a potential detection mechanism for gene therapy.

#### 4.3. DIACEST pH imaging

Changes in pH appear in several biological processes such as apoptosis [132] and for several pathologies, including stroke [133–135], cancer [136–140], and hyperglycemia [141,142]. Because proton exchange depends strongly on pH, CEST provides a unique and extremely useful approach for water-based pH MRI. In fact, pH imaging has become a central topic for CEST and is being evaluated by many researchers. Previous pH approaches for MR have mainly relied on spectroscopy, the most well known being phosphorus ( $^{31}\text{P}$ ) MRS [143–146]. However, this approach has very low spatial resolution (20–30 ml) and is not applicable in standard clinical MRI scanners, which are limited predominantly (>99%) to proton MRI studies. Proton spectroscopy of several types of exogenous and endogenous protons has also been shown to allow sensitive detection of pH changes in vivo. Examples of these are imidazole protons in 2-imidazol-1-yl-3-ethoxycarbonyl-propionate (IEPA) [147–150] and in histidine [151], which have a

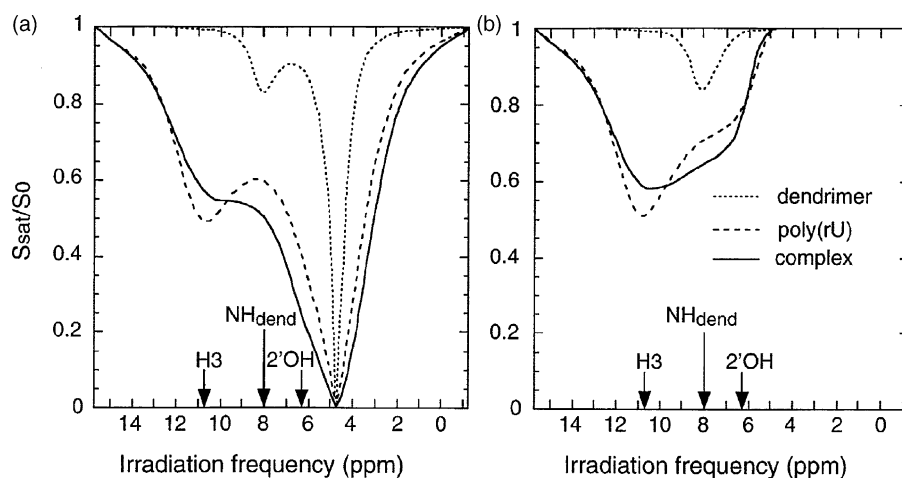


Fig. 14. (a) 500 MHz  $^1\text{H}$  z-spectra of 5  $\mu\text{M}$  poly(rU), 100  $\mu\text{M}$  G-5 dendrimer, and 100  $\mu\text{M}$  dendrimer/10  $\mu\text{M}$  poly(rU) complex. (b) Asymmetry analysis of z-spectra. The three contributions to the water signal saturation can be assigned to the poly(rU) imino proton H3, poly(rU) hydroxyl proton 2'OH, and dendrimer amide proton NH. Irradiation power 1 mW, 37  $^\circ\text{C}$ , pH 7.3. Reprinted from [21], with permission from Wiley-Liss, Inc.

chemical shift dependency on pH. In 1998, Mori et al. [116] for the first time proposed the use of exchangeable amide protons in mobile proteins and peptides for detection of in vivo pH changes using MRS. However, this has not been applied in the clinic due to acquisition time limitations and low spatial resolution. A few pH-sensitive contrast agents have been developed that can be used for standard proton MRI [152,153], but again these have not found any application in the clinic.

In 2000, Ward et al. [19] reported the pH dependence of the CEST spectra of 5,6-dihydrouracil, barbituric acid, and many other small molecules in solution. To demonstrate the power and resolution of this new approach, they obtained CEST images of a phantom containing several compartments with barbituric-acid solutions of different pH (6.5, 7.0, and 7.4), a control solution, and water. Subsequently, van Zijl et al. [81] demonstrated that compounds containing amide protons, such as PLL and SPD-5, are very suitable CEST contrast agents for pH imaging in the physiological range. Snoussi et al. [21] reported that the exchange rate of the poly(rU) imino protons is  $1213\text{ s}^{-1}$  at pH 7 and  $15^\circ\text{C}$ ,  $3080\text{ s}^{-1}$  at pH 7 and  $37^\circ\text{C}$ , and  $5880\text{ s}^{-1}$  at pH 7.3 and  $37^\circ\text{C}$ . This pH dependence of the exchange rates of the amide protons and imino protons is characteristic of exchange catalyzed by  $\text{OH}^-$  (base-catalysis). Recently, McMahon et al. [76] carefully detailed the exchange properties and pH dependencies of several amide-proton containing compounds. It was shown that, when using such compounds, great care has to be taken for their proper calibration. For instance, if the exchange rate gets too high (e.g. at higher pH), the simplified approximations used to derive Eq. (20) may no longer hold, and erroneous exchange rates will be obtained. Special care should therefore be taken for conditions of very fast exchange, a high solute concentration, or a very high magnetic field, under which  $k_{\text{ws}}$  (back transfer of water protons to solute protons) may become comparable in magnitude with  $R_{1\text{w}}$ . In the ultimate case of  $k_{\text{ws}} \gg R_{1\text{w}}$ , the proton transfer ratio will become independent of the exchange rate (see the third equality of Eq. (20)), and CEST MRI will no longer be able to achieve pH-sensitive image contrast.

Another potential problem for the use of CEST imaging for pH detection is that CEST contrast depends on multiple parameters, including exchangeable site concentration, ionic strength, temperature, and water content, and probably some other factors influencing the chemical environment of the exchangeable protons. CEST contrast also depends on several MRI parameters, especially  $R_{1\text{w}}$ , and experimental parameters such as the RF irradiation power and frequency. To quantify pH, it is necessary to evaluate and/or exclude these other contributions. One possibility for proper pH quantification is the use of an internal standard. This approach was applied by Ward and Balaban [80], who proposed a ratiometric technique to remove the contributions of contrast agent concentration and  $R_{1\text{w}}$ . This approach requires two or more exchangeable sites with different chemical shifts and pH dependencies. These exchange sites can be in the same molecule or different molecules. In the limit of negligible back exchange and complete saturation of the exchangeable protons, the PTR ratio

of the two sites varies only with the ratio of the exchange rates, which can then be used for pH calibration. Ward and Balaban [80] evaluated the potential of this technique for a combination of 5-hydroxytryptophan and 2-imidazolidinethione as well as for 5,6-dihydrouracil (Fig. 15). The two exchangeable protons in 5,6-dihydrouracil (site 1 at 5.00 and site 2 at 2.67 ppm from water), each have a specific pH dependence. When plotting the ratio  $M_{\text{S}}^{\text{site 2}}(M_0 - M_{\text{S}})^{\text{site 1}} / [M_{\text{S}}^{\text{site 1}}(M_0 - M_{\text{S}})^{\text{site 2}}]$  as a function of pH, a singular, hyperbolic standard pH curve was found with exquisite sensitivity in the 6.2–7.2 pH range (Fig. 15b).

#### 4.4. DIACEST reporter genes

Recently, a field of molecular imaging has emerged in which the goal is to reach molecular-type sensitivities for imaging. For MRI, one of the goals is to design so-called MR reporter genes, which have the potential to provide information on the biodistribution and viability of transfected cells in vivo. Currently, such genes have relied on the administration of paramagnetic or superparamagnetic substrates [154,155]. This has the disadvantage of a label that cannot be distinguished from in situ magnetic field inhomogeneities and cannot be turned off. The property of agents that they can be switched on and off repeatedly at will by applying a frequency-selective

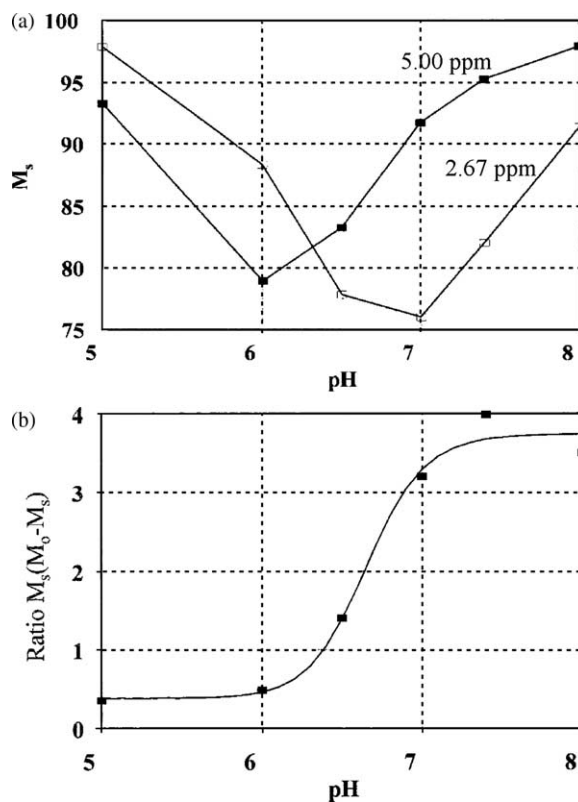


Fig. 15. Ratiometric approach to quantify pH using CEST based on two base-catalyzed exchange sites from 5,6-dihydrouracil (62.5 mM). These two exchange sites are site 1 at 2.67 ppm and site 2 at 5.00 ppm from the water resonance, which show different pH-dependent CEST properties (a). The ratio  $M_{\text{S}}^{\text{site 2}}(M_0 - M_{\text{S}})^{\text{site 1}} / [M_{\text{S}}^{\text{site 1}}(M_0 - M_{\text{S}})^{\text{site 2}}]$  shows a hyperbolic pH dependence with optimum sensitivity in the physiological range (b). Modified from [80], with permission from Wiley-Liss, Inc.

irradiation pulse therefore provides a unique new tool for the design of such reporters. Very recently, Gilad et al. [84] reported the design, cloning and expression in mammalian cells of an artificial CEST reporter gene encoding for a lysine rich protein (LRP, 200 lysine residues, 32 kDa). To demonstrate the potential of this approach, 9L rat gliosarcoma cells were transfected with the vector encoding to the LRP gene. Reference cells with an empty vector containing only EGFP were also prepared. A 5 mm NMR tube was filled with phosphate buffer solution (PBS) contained capillaries with (i) PLL 30 kDa 10  $\mu$ M, (ii) PLL 30 kDa 100  $\mu$ M, (iii) protein extract from 9L-LRP cells, (iv) protein extract from control cells transfected with empty vector, and (v) PBS only. MRI experiments at 500 MHz and at physiological temperature and pH showed that the protein extract from cells expressing LRP had an average change in the signal intensity of 1.33% ( $P=0.00064$ ) while the protein extract from control cells showed no effect ( $-0.13\%$ ,  $P=0.65$ ). Moreover, pixel-by-pixel  $t$ -test maps (comparing the set of images saturated at  $\pm 3.76$  ppm) showed a significant change in MR signal in the capillary containing LRP, while nothing was detected in the control capillaries. Subsequently, it was shown that the reporter gene could be detected in vivo. This first artificial CEST gene experiment showed the potential to use CEST for tracking cells in vivo without the need for an exogenous substrate. Importantly, the gene provided a detectable MR contrast that was independent of cell division and visible only following a specific frequency-selective saturation pulse. It is expected that more efficient reporter genes will be designed in the near future.

## 5. Paramagnetic chemical exchange dependent saturation transfer (PARACEST)

A successful CEST experiment is bound by the condition that the exchangeable proton needs to be selectively irradiated. Consequently, the system has to be in slow or intermediate exchange on the NMR time scale ( $\Delta\omega_{\text{sw}} \geq k_{\text{sw}}$ ). This limits the highest possible exchange rate useable for diamagnetic systems to the order of 1000 Hz, because the proton chemical shifts are typically within 6 ppm (i.e. 383, 1200 and 3000 Hz at 1.5, 4.7 and 11.7 T, respectively) from the bulk water resonance. Obviously, the use of high magnetic fields is of great advantage to CEST measurements, but possible increases in field strength are very limited. On the other hand, paramagnetic shift agents [22–24] are able to effectively enlarge the chemical shift of the exchange site by several orders of magnitude and thus provide an alternative approach to attain slow-intermediate exchange NMR conditions even for very high exchange rates (Table 1). Moreover, some concomitant disturbing effects such as conventional solid-like macromolecular MT and direct RF saturation can be reduced or even completely avoided. Recently, an early review discussing the PARACEST agents has appeared [64], outlining much of the essential properties. We here summarize some of the main results.

### 5.1. PARACEST effects

Using lanthanide complexes, Zhang and Sherry [22,23] were the first to demonstrate the use of paramagnetic complexes for CEST imaging. They exploited the fact that, contrary to the widely-used  $\text{Gd}^{3+}$ -based MRI contrast agents, several lanthanide complexes have unusually slow bound water exchange properties [130,131]. Based on the particular suitability of their proton chemical shifts and lifetimes of  $\text{Ln}^{3+}$ -bound water, Zhang et al. [22,23] chose to perform experiments on the Ln-DOTA-4AmCE complexes of Pr, Nd, Eu and Yb (Table 1). At the field strength used, 4.7 T, the estimated product  $\Delta\omega_{\text{sw}}\tau_{\text{s}}$  was 24, 3.2, 1.5 and 0.8 for  $\text{Eu}^{3+}$ -,  $\text{Nd}^{3+}$ -,  $\text{Pr}^{3+}$ - and  $\text{Yb}^{3+}$ -bound water, respectively. Three of these fall in the slow to intermediate exchange range ( $\Delta\omega_{\text{sw}}\tau_{\text{s}} \geq 1$ ). Fig. 16 shows the MT profiles for 63 mM solutions of the Eu and Nd complexes, for which CEST peaks appear at 50 and  $-32$  ppm, respectively. They found that Eu-DOTA-4AmCE appears to be the most favorable PARACEST agent at 25  $^{\circ}\text{C}$ , showing the largest effect ( $\sim 57\%$ ) on the bulk water signal. The CEST peak is much broader in Nd-DOTA-4AmCE than in Eu-DOTA-4AmCE, because its water exchange is faster (lifetime: 80 vs. 382  $\mu\text{s}$ ). In comparison with  $\text{Eu}^{3+}$  and  $\text{Nd}^{3+}$ , a lower but detectable CEST effect (shifted toward water) was observed for Pr-DOTA-4AmCE, while no CEST effect was detected for Yb-DOTA-4AmCE, as expected. Zhang and Sherry [23] further noticed that there was a large decrease in  $z$ -spectrum intensity even when RF irradiation was applied at mid-frequency between the bound and bulk water resonances.

Aime et al. [24] explored the CEST properties of another series of lanthanide(III) complexes (Ln = Eu, Dy, Ho, Er, Tm, Yb) with the macrocyclic DOTAM-Gly ligand at 7.05 T. There are two kinds of exchangeable protons in these chelates, namely, coordinated water and amide protons. The chemical shifts of the amide protons are distributed between  $-51$  and  $77$  ppm from the water resonance (Table 1). The NH resonance (16 ppm upfield from the  $\text{H}_2\text{O}$  signal) of Yb-DOTAM-Gly has the best CEST property (Fig. 17a) in that 70% suppression of the water signal can be obtained at pH 8.1 and 312 K. The amide NH protons in Eu-DOTAM-Gly ( $-4$  ppm from the water resonance) could not be distinguished from direct saturation effects, because too strong RF saturation (25  $\mu\text{T}$ ) was applied. When carrying out experiments as a function of Yb-DOTAM-Gly concentration, Aime et al. [24] found an absence of a linear dependence between the magnitude of the CEST effect and the concentration of the agent. This can probably be explained by taking several factors into account, especially back exchange and direct water saturation.

Another way to use paramagnetic agents for CEST imaging is to use them as NMR shift reagents for exchanging protons or to create a magnetic susceptibility difference between physical compartments [156,157]. For example, Aime et al. [157] recently reported a highly sensitive CEST system using liposomes, which he dubbed LIPOCEST. In such systems, the resonance of the water protons inside the liposomes is shifted from that of the external water by the shift agent entrapped within the liposomes. In the presence of 0.19 M

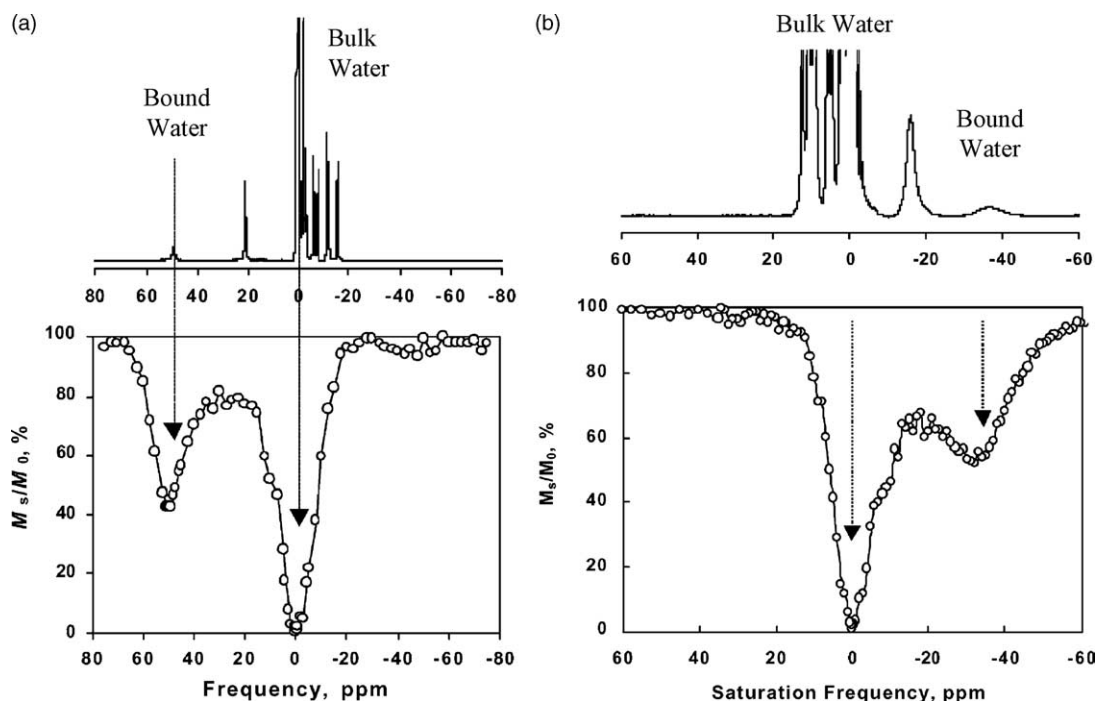


Fig. 16. z-Spectra of Eu-DOTA-4AmCE (a) and Nd-DOTA-4AmCE (b) obtained at 4.7 T (63 mM, pH 7, room temperature, saturation power 16.4 dB, saturation time 1 s). The CEST peaks of the complexes appear near +50 ppm for Eu-DOTA-4AmCE and -32 ppm for Nd-DOTA-4AmCE. The bulk water signal is reduced by ~57 and 48%, respectively. The bound water resonances are clearly visible in the 500 MHz <sup>1</sup>H NMR spectra, indicating fulfillment of the slow exchange regime. Modified from [22,23], with permission from American Chemical Society and Elsevier Science (USA), respectively.

[Tm(dotma)]<sup>−</sup> (where DOTMA =  $\alpha, \alpha', \alpha'', \alpha'''$ -tetramethyl-1,4,7,10-tetraacetic acid), the water signal in the liposome displays a separate resonance at 3.1 ppm downfield from the signal of bulk water (312 K), indicating sufficiently slow exchange between the compartments. Even though the difference in the chemical shift between the two water resonances is small, the LIPOCEST agent could be detected down to a concentration of about 90  $\mu$ M.

## 5.2. PARACEST agents for pH reporting

Aime et al. [24] found that the CEST effect for the amide protons in the Yb-DOTAM-Gly complex (30 mM, 312 K) is

markedly pH-dependent, indicating a linear pH dependence in the pH range of 5.5–8.1. The potential application of Yb-DOTAM-Gly as a pH responsive CEST contrast agent is shown in Fig. 17(b). The noticeable contrast difference among the four samples outlines the excellent pH sensitivity of this PARACEST agent. To quantify pH using PARACEST, Aime et al. [24] tested the feasibility of the ratiometric approach [80] on the lanthanide complexes. They prepared a mixture containing 20 mM of the Yb-DOTAM-Gly complex and 16 mM of the Eu-DOTAM-Gly complex, and examined the CEST effects associated with the amide NH protons for Yb-DOTAM-Gly (ca. 16 ppm upfield from the bulk water peak) and the metal coordinated water protons for Eu-DOTAM-Gly (ca. 40 ppm

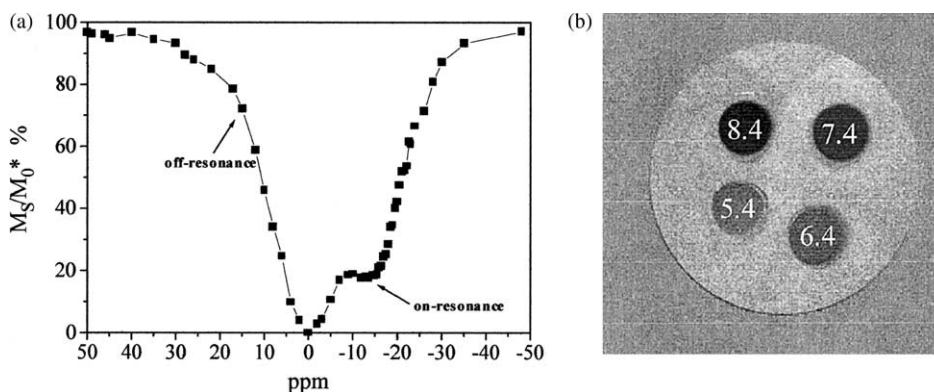


Fig. 17. (a) A CEST spectrum of Yb-DOTAM-Gly obtained at 7.05 T (30 mM, pH 8.1, 312 K, irradiation time 4 s, irradiation power 25  $\mu$ T). (b) A CEST image of a phantom of four vials of Yb-DOTAM-Gly at 7.05 T (30 mM, 298 K). The saturation pulse (power 12  $\mu$ T, time 4 s) was centered first on the amide protons (-4794 Hz from bulk water) and then symmetrically with respect to the water resonance (+4794 Hz from bulk water). The CEST image that is pH-weighted is the difference between two  $T_1$ -weighted images (TR=3.04 s, TE=18.3 ms). Reprinted from [24], with permission from Wiley-Liss, Inc.



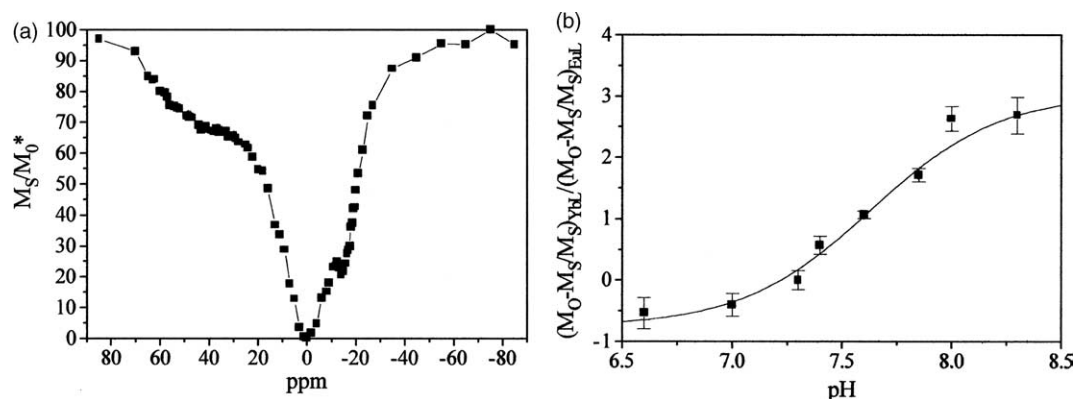


Fig. 18. (a) CEST spectra of a mixture of 16 mM Eu-DOTAM-Gly and 20 mM Yb-DOTAM-Gly at pH 8.1. (b) pH dependence using the ratiometric method.  $B_0 = 7.05$  T, 312 K, irradiation time 4 s, and irradiation power 25  $\mu$ T. Reprinted from [24], with permission from Wiley-Liss, Inc.

downfield from the water resonance). Fig. 18 shows the z-spectrum acquired at pH 8.1 and the pH dependence of the ratio  $[(M_0 - M_S)/M_S]_{YbL} / [(M_0 - M_S)/M_S]_{EuL}$ . Thus, the sensitivity of the method is very good in the pH range of 6.5–8.5. Subsequently, Aime et al. [82,83] tested the ratiometric method for the same paramagnetic DOTAM-Gly complex of the lighter  $\text{Ln}^{\text{III}}$  ions (Pr, Nd, and Eu). Although these three complexes show ratiometric plots of similar shape, the calculated curve and, consequently, the accuracy and the sensitivity of the pH responsiveness, is considerably higher for the  $\text{Pr}^{\text{III}}$  complex. Interestingly, the marked pH dependence observed for these systems is basically due to the pH dependence of the amide proton exchange, while the CEST effect arising from the coordinated water protons is basically unaffected in the investigated pH range.

Zhang et al. [158] quantitatively measured the exchange properties of the amide protons for the lanthanide complexes at 7.05 T and found that these sites meet the slow-exchange condition in a wide pH range. Their experimental results clearly show that the CEST effects of the amide protons in the lanthanide complexes are pH-dependent, and potentially suitable as pH reporters.

### 5.3. Metabolite detection

The CEST properties of paramagnetic lanthanide complexes can be made sensitive to the presence of particular metabolites. The first example of this was given by Aime et al. [78], who demonstrated the detection of lactate using a  $[\text{Yb}(\text{MBDO3AM})]^{3+}$  complex that has a preference for binding anions. The NMR spectrum of a solution containing this complex and L-lactate (4:1 ratio) shows signals of both the free and lactate-bound form of the chelate. The amide protons of free chelate have a broad resonance at  $-28.5$  ppm (width of  $\sim 1500$  Hz at pH 6.4 and 298 K), whereas the same protons for the bound species show two narrower doublets (width of  $\sim 300$  Hz), resonating between  $-14$  and  $-20$  ppm. The exchange between the two species is slow on the NMR time scale. The z-spectra (Fig. 19a) for the two forms of the complex at 312 K and pH 7.4 overlap partially, mainly due to a severe broadening of the amide proton signals at higher pH and temperature. To

saturate as selectively as possible, the irradiation of the amide protons of the free chelate was directed to  $-29.1$  ppm, whereas the bound form was irradiated at  $-15.5$  ppm. The measured saturation transfer values (Fig. 19b) for the amide protons of the free complex have a strong dependence on the lactate concentration in the 0–10 mM range, while this is much reduced when the amide protons of the lactate-bound complex

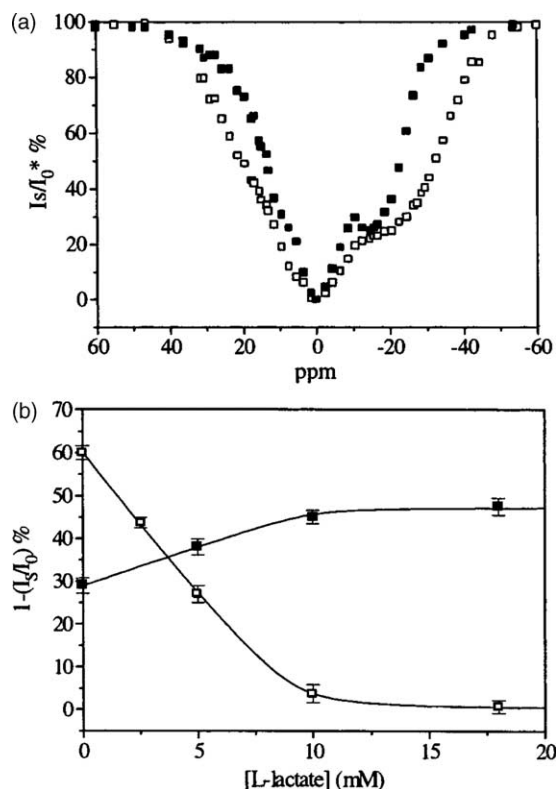


Fig. 19. (a) CEST spectra of a 30 mM solution of  $[\text{Yb}(\text{MBDO3AM})]^{3+}$  complex: free ( $\square$ ) and fully bound to L-lactate ( $\blacksquare$ ). (b) CEST effect for a 9.3 mM solution of  $[\text{Yb}(\text{MBDO3AM})]^{3+}$  as a function of L-lactate concentration. The irradiation was set to the amide frequency corresponding to free ( $-29.1$  ppm,  $\square$ ) and L-lactate bound ( $-15.5$  ppm,  $\blacksquare$ ) complex. pH 7.4, 312 K, irradiation power 25  $\mu$ T, irradiation time 6 s, and  $B_0$  7.05 T. Marks ( $\blacksquare$  and  $\square$ ) were adjusted to be consistent between the two combined figures. Modified from [78], with permission from American Chemical Society.



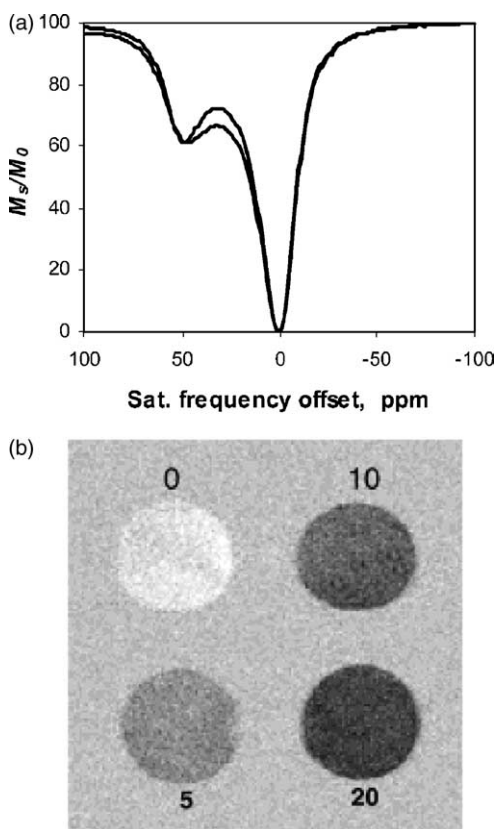


Fig. 20. (a) z-Spectra at 4.7 T of 10 mM Eu-DOTA-4Am ligand with bis(phenyl boronate) arms in the absence (lower curve) and presence (upper curve) of 20 mM glucose. The bulk water signal in the sample containing only complex decreased  $\sim 38\%$  at the bound water position ( $\sim 50$  ppm). (b) CEST images of a phantom of four plastic tubes containing 10 mM complex and either 0, 5, 10, or 20 mM glucose, showing the possibility to image metabolite concentrations. pH 7.0, 25 °C, irradiation time 2 s, and irradiation strength 1020 Hz. Reprinted from [79], with permission from American Chemical Society.

are irradiated. These plots were used to determine the equilibrium constant ( $8 \times 10^3$ ) and the amide proton exchange rate of the free complex ( $1180 \text{ s}^{-1}$ ). Using this method, it is possible to determine lactate concentrations under the conditions of a known contrast agent concentration and a  $[\text{Lac}]/[\text{complex}]$  smaller than one.

The second example of the use of a PARACEST agent for metabolic mapping by MRI was demonstrated by Zhang et al. [79]. They used a Eu-DOTA-4Am ligand with bis(phenyl boronate) arms that binds to glucose and showed that the exchange-slowing upon binding can be used as a glucose probe. Although a similar CEST effect (Fig. 20a) was observed at the peak maximum ( $\sim 50$  ppm) for both free complex and the glucose mixtures, the shape of the z-spectra upon binding changes between 25 and 35 ppm upon glucose addition. This is consistent with the prediction that the binding of glucose slows exchange of the  $\text{Eu}^{3+}$ -bound water molecule. A plot of the ratio of  $M_s(30 \text{ ppm})/M_s(50 \text{ ppm})$  vs. glucose concentration shows that the most responsive range for detection of glucose is 0–20 mM. To illustrate the potential for imaging glucose concentration, the investigators built a phantom consisting of four plastic tubes each containing 10 mM complex and different amounts of glucose. Images were acquired by alternatively applying presaturation pulses at 50 and 30 ppm. The difference images (Fig. 20b) show clear intensity gradations that parallel the glucose concentration.

#### 5.4. PARACEST agents for cell labeling

The possibility of tunable imaging of cells labeled with PARACEST agents was recently demonstrated by Aime et al. [159] using metal complexes of Eu and Tb with the dotamGly ligand. As mentioned above, such complexes contain two pools of exchangeable species: the metal coordinated water and the amide protons. The presence of PARACEST agents in cells was visualized by using the large water shifts. Cell labeling was carried out by incubation of  $\sim 10^6$  HTC (rat hepatoma) tumor cells in the presence of Eu(dotamGly) or Tb(dotamGly) (40 mM) in the incubation medium for 6 h. Incubated cells were collected as pellets and a 4-vial phantom was prepared comprised of four pellets: (A) unlabeled HTC cells, (B)  $\text{Tb}^{\text{III}}$ -labeled cells, (C)  $\text{Eu}^{\text{III}}$ -labeled cells, and (D) a mixture of  $\text{Tb}^{\text{III}}$ - and  $\text{Eu}^{\text{III}}$ -labeled cells. MR images of the phantom were acquired at 7.05 T. Each CEST image is the difference of two spin echo images that differ in the offset of the irradiation pulse. Cells that contained  $\text{Tb}^{\text{III}}$  complex were detected by irradiation at 600 ppm, whereas  $\text{Eu}^{\text{III}}$ -complex-containing cells were

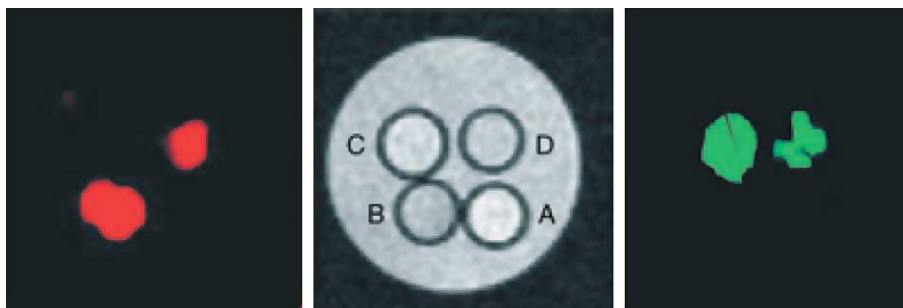


Fig. 21. Imaging at 7 T of selective cell labeling with two PARACEST probes. Four capillaries are: (A) unlabeled HTC cells, (B) HTC cells labeled with Tb(dotamGly), (C) HTC cells labeled with Eu(dotamGly), and (D) cellular pellet obtained from a mixture of pellets of spots (B) and (C). Middle: a reference image without saturation. Left and right: CEST difference images obtained by irradiation of the metal bound water protons of Tb(dotamGly) (600 ppm) and Eu(dotamGly) (50 ppm), respectively. The total irradiation time was 2 s (sinc3 pulse train, irradiation power  $\sim 250 \mu\text{T}$ , duration 1 ms for the  $\text{Eu}^{\text{III}}$  complex and 250  $\mu\text{s}$  for the  $\text{Tb}^{\text{III}}$  complex, delay 10 ms). Reprinted from [159], with permission from Wiley-VCH Verlag GmbH & Co. KGaA, Weinheim.

selected by switching the irradiation frequency to 50 ppm (Fig. 21). The decreases in the water signal intensities were 4% (pellet D) and 12% (pellet C) upon irradiation at  $\pm 50$  ppm, and 3.5% (pellet D) and 11.2% (pellet B) upon irradiation at  $\pm 600$  ppm, showing good potential for this type of cell labeling.

### 5.5. Temperature measurement

The magnitude of the CEST effects strongly depends on the temperature, and CEST imaging therefore may provide a direct measure of temperature if the concentration of the agent and other contributions to the effects are known. No reports using signal magnitude have yet appeared. However, Zhang et al. [160] recently proposed an alternative way that PARACEST agents could be used as a novel probe for MR thermometry. As reported previously [23], the  $^1\text{H}$  chemical shifts of lanthanide bound water ( $\text{Ln-H}_2\text{O}$ ) range from +500 ppm for  $\text{Tm}^{3+}$  complex to  $-720$  ppm for  $\text{Dy}^{3+}$  complex. They found that the  $^1\text{H}$  chemical shifts ( $\delta$ , in ppm) of  $\text{Ln-H}_2\text{O}$  complexes change linearly with temperature in a physiological temperature range, namely,  $\delta = -0.4 \text{ T} + 64.6$  and  $\delta = 6.9 \text{ T} - 944.7$  for Eu- and Dy-DOTA-tetraamide complexes, respectively. Thus, the  $^1\text{H}$  chemical shifts of  $\text{Ln}^{3+}$ -bound water molecules or the peaks of the CEST spectra of the complex can be used to determine the temperature according to these linear calibrations. To test the feasibility of the method, Zhang et al. [160] prepared a vial containing 10 mM Eu-DOTA-4AmC in water (pH 7) and acquired a series of CEST images over a small range of frequencies around the  $\text{Eu}^{3+}$ -bound water resonance (50 ppm). A minimum in  $M_S/M_0$  was determined on a pixel-by-pixel basis, and the temperature was calculated from the frequency at this minimum. The results showed that small temperature gradients across the vial (1 cm OD) could be detected easily. The temperature response sensitivity of these agents is about 40-fold (Eu: 0.4 ppm per  $^\circ\text{C}$ ) and 690-fold (Dy: 6.9 ppm per  $^\circ\text{C}$ )-fold greater, respectively, than the traditional proton resonance frequency method (0.01 ppm per  $^\circ\text{C}$ ). In addition, because bulk water (55.5 M) is imaged, the spatial resolution would be much higher than that possible using MRS of shift reagents. Similar to other applications discussed in this review, this method will have to deal with conventional MT effects,  $B_0$  field homogeneity, and specific absorption rate (SAR) issues when applying it in vivo.

## 6. Amide proton transfer (APT) imaging

Zhou et al. [25,26] recently demonstrated that it is possible to produce CEST contrast reflecting properties of the amide protons in endogenous mobile proteins and peptides. Although these protons were detected earlier by Mori et al. [116] using MRS, the use of their properties for clinical diagnosis and prognosis was not possible due to their very low concentration in tissue. Zhou et al. demonstrated that, although the concentration of these tissue proteins and peptides is only in the millimolar range, it is possible to achieve a detection sensitivity of several percent on the water signal (molar concentration). This CEST enhancement scheme for the amide

protons in endogenous proteins and peptides was called APT imaging. In this section, we review this technology and discuss the possibility to add intrinsic pH contrast as well as protein and peptide-content contrast as non-invasive diagnostic tools for clinical imaging.

### 6.1. In situ APT effects

APT effects in vivo were first demonstrated on the rat brain in situ at 4.7 T by Zhou et al. [25]. Fig. 22(a) and (b) shows z-spectra acquired under different physiological conditions, in vivo (normocapnia and hypercapnia) and postmortem. Even though the effects of direct water saturation and conventional MT dominate the spectra, the existence of APT effects is indicated by a very small dip in intensity at a frequency difference of +3.5 ppm from water (dotted vertical line). This frequency corresponds to about 8.3 ppm in the proton spectrum, where the amide protons resonate. The presence of APT effects becomes clear when comparing the in vivo and postmortem spectra. Interestingly, the MT curves coincide on the negative-offset side of water, but not on the positive-offset side, where the exchangeable protons resonate. When keeping in mind that decreased pH leads to a decreased proton exchange rate, the reduced saturation transfer in the postmortem brain can be explained. During hypercapnia (Fig. 22b), an upward shift of the total MT curve is visible. This was attributed to BOLD effects due to increased blood volume upon hypercapnia, an effect that was recently quantified [99]. When applying an MT asymmetry analysis to remove direct saturation and conventional MT effects, the resulting curves (Fig. 22c) show a varying MT difference that is initially positive and then negative. When extending the irradiation range (Fig. 22d), the  $\text{MTR}_{\text{asym}}$  curve levels off at about  $-3\%$  for higher offsets. This finding supported a previous report by Pekar et al. [100] that the solid-like MT effect is asymmetric with respect to the water resonance (see also Eqs. (24) and (25)). Thus, to observe true proton transfer effects, an additional reference may be needed. For instance, when subtracting the normocapnic  $\text{MTR}_{\text{asym}}$  plot from the postmortem curve, a maximum signal change is found exactly at an offset of 3.5 ppm from water (Fig. 22e and f), indicating that this difference originates predominantly from the amide protons of the mobile proteins and peptides. Therefore, similar to Eq. (25), we have

$$\text{MTR}_{\text{asym}}(3.5 \text{ ppm}) = \text{MTR}'_{\text{asym}}(3.5 \text{ ppm}) + \text{APTR} \quad (31)$$

in which  $\text{MTR}'_{\text{asym}}(3.5 \text{ ppm})$  is the inherent asymmetry of the solid-phase MT effect associated with immobile macromolecules and membranes, and APTR is the amide proton transfer ratio for the amide protons associated with mobile cellular proteins and peptides.

Zhou et al. [25] performed APT imaging experiments on the rat brain at 4.7 T. In addition to the relaxation rates, they measured the amide proton exchange rate [25,75] using WEX spectroscopy, which could be used to determine that saturation was almost complete ( $\alpha = 0.987 \approx 1$ ). In addition, they used a long RF saturation time of 4 s ( $\sim 3T_{1w}$ ), which is sufficient to

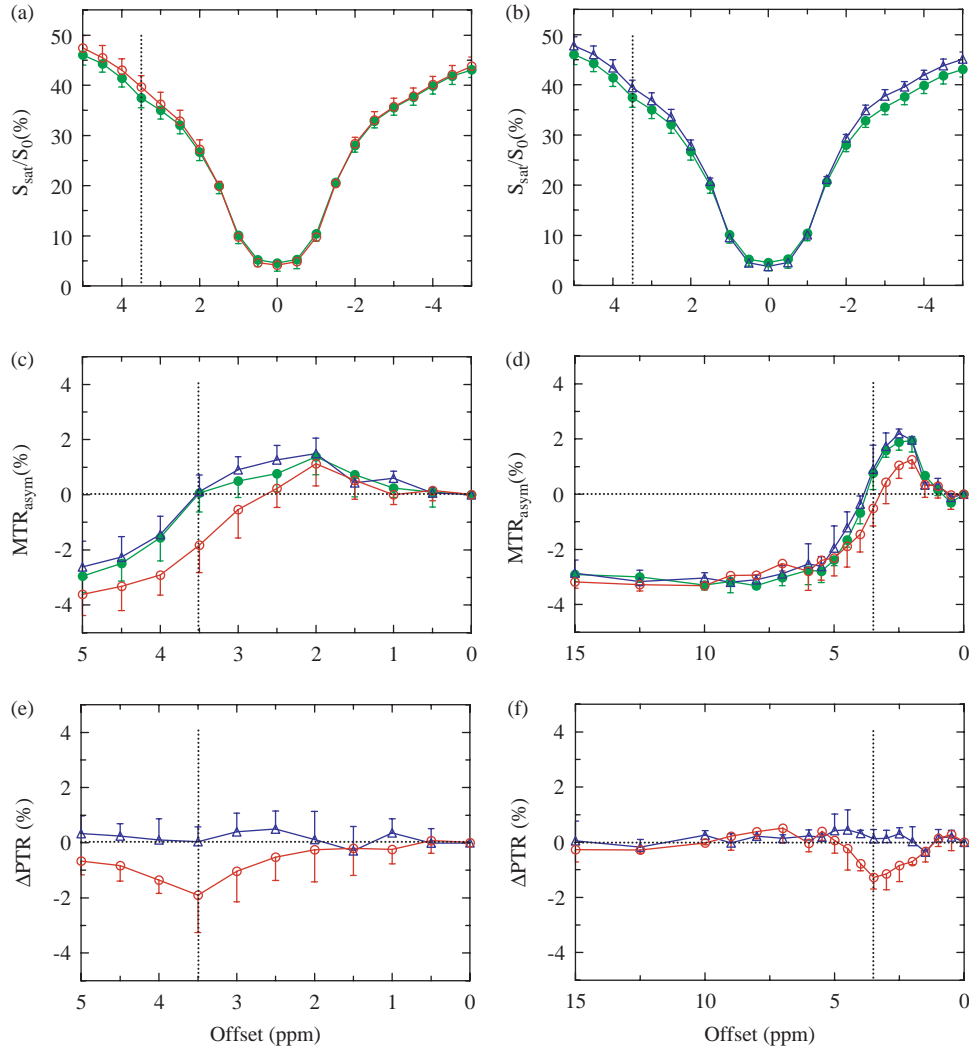


Fig. 22. z-Spectra,  $MTR_{\text{asym}}$  spectra, and  $\Delta PTR$  spectra at 4.7 T for the rat brain ( $n=7$ ) during normocapnia (●), hypercapnia (△), and cardiac arrest (○). The small dip at offset 3.5 ppm during normocapnia and hypercapnia ((a) and (b)) corresponds to the spectral amide frequency around 8.3 ppm. The  $MTR_{\text{asym}}$  spectra ((c) and (d)) and  $\Delta PTR$  spectra ((e) and (f)) show that postmortem changes are only visible in the 0–5 ppm offset range from water. Reprinted from [25], with permission from the authors and Nature Publishing Group.

obtain maximum saturation transfer. Because, for these endogenous amide protons,  $k_{\text{ws}}$  is negligible compared with  $R_{1\text{w}}$  ( $k_{\text{ws}} \approx 0.02 \text{ s}^{-1}$ ,  $R_{1\text{w}} \approx 0.7 \text{ s}^{-1}$ ), Eq. (20) for PTR can be rewritten as

$$\text{APTR} = \frac{k_{\text{sw}}[\text{amide proton}]}{R_{1\text{w}}[\text{water proton}]} (1 - e^{-R_{1\text{w}} t_{\text{sat}}}) \quad (32)$$

in which  $k_{\text{sw}}$  should be thought of as the average exchange rate for all amide protons participating in the effect. Thus, APT contrast depends on several MR (water spin–lattice relaxation rate) and tissue (exchangeable amide proton concentration, water content, amide proton exchange rates) related parameters. Because water content and  $R_{1\text{w}}$  change for many pathologies, APT contrast can only be specific if the effects of exchangeable amide proton concentration and exchange rates in lesions outweigh the others. Fortunately this is sometimes the case, and the use of APT imaging was recently demonstrated for non-invasive ischemia detection [25] and cancer imaging [26]. In these animal experiments, APTR

decreased by 1–3% [25] during middle cerebral artery (MCA) occlusion and increased by 3–4% [26] in an experimental rat brain tumor. These results were interpreted as being predominantly caused by decreased amide proton exchange rates (or decreased intracellular pH) during ischemia and increased amide proton content in the brain tumors, respectively.

## 6.2. pH Imaging using APT

Using the in situ rat data and Eq. (32), Zhou et al. [25] established a two-point pH calibration curve at 4.7 T. This could be accomplished because of the finding of negligible changes in the combined effects for water content and  $R_{1\text{w}}$  during the first two hours after cardiac arrest. In addition, it was determined that the amide proton content also remains constant in this early postmortem period, while the amide proton exchange rate changes from  $28.6 \pm 7.4 \text{ s}^{-1}$  in vivo to  $10.1 \pm 2.6 \text{ s}^{-1}$  postmortem [25,75]. Using  $\Delta \text{APTR}$  (−1.90%) and the

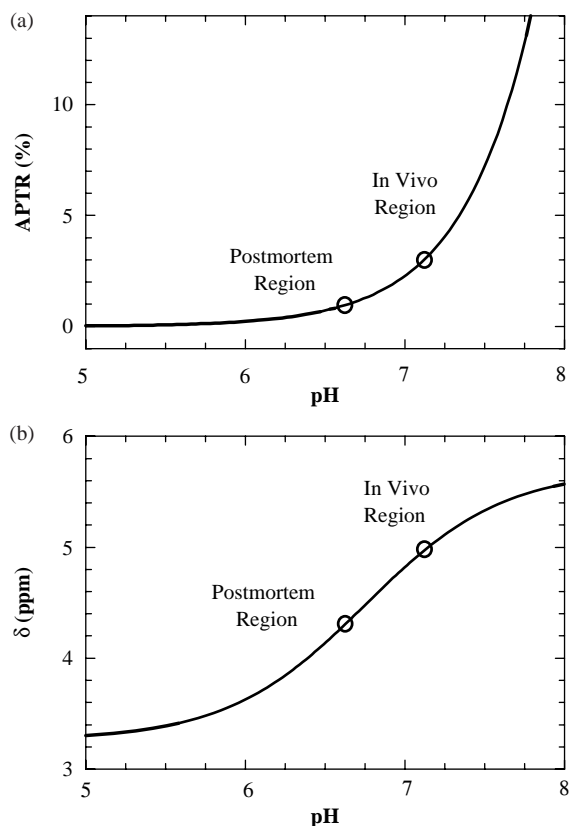


Fig. 23. (a) Calculated APTR–pH relationship for the in situ rat brain at a magnetic field strength of 4.7 T. (b) Calculated  $\delta$ –pH curve for phosphorous spectroscopy based on the equation:  $\text{pH} = 6.75 + \log[(\delta - 3.26)/(5.70 - \delta)]$ . Reprinted from [85], with permission from Wiley-Liss, Inc.

measured rates, the total amide proton concentration from all proteins and peptides could be calculated to be about 71.9 mM, leading to APTR values at the 3.5 ppm offset of 2.94% at normocapnia and 1.04% postmortem. Because of the lack of change in amide signal intensity, the APTR change was due to the pH reduction upon death ( $\text{pH } 7.11 \pm 0.13$  at normocapnia

and  $6.66 \pm 0.10$  postmortem,  $n=7$ , as measured using  $^{31}\text{P}$  spectroscopy; base-catalyzed for pH values above  $\sim 5$ ,  $k_{\text{sw}} \propto 10^{\text{pH}}$ ). Based on Eq. (32), it can be seen that APTR is a direct function of pH, with a dependency on field strength (because of  $R_{1w}$ ). The calibrated APTR–pH relationship was determined to be:

$$\text{APTR} = 5.73 \times 10^{\text{pH}-9.4} \quad \text{or} \quad \text{pH} = 9.4 + \log(\text{APTR}/5.73). \quad (33)$$

Fig. 23 compares this two-point calibration with the one from  $^{31}\text{P}$  spectroscopy, in which tissue intracellular pH is quantified according to the chemical shift difference between inorganic phosphate and phosphocreatine. It was concluded [85] that the sensitivity for measuring pH changes in the physiological range (pH 6.5–7.5) is quite good, showing an APTR reduction by 65% between normal and postmortem brain tissue. Compared to  $^{31}\text{P}$  spectroscopy, this is a larger relative change than in the chemical shift difference, but it may not be as easy to detect. On the other hand, chemical shift measurements of the inorganic phosphate peak are often compromised by overlapping phosphomonoesters, and spatial resolution of  $^{31}\text{P}$  imaging and spectroscopy is limited.

As a first application of APT pH imaging, Zhou et al. [25] studied permanent ischemia in the rat brain using a middle cerebral artery occlusion (MCAO) model. It was found that the  $\text{MTR}_{\text{asym}}$  spectra for contralateral and ipsilateral regions compare very well with those for in vivo and postmortem brain, respectively, showing a reduction in intensity for the 2–5 ppm offset range, indicating that this particular ischemic brain model shows a pH decrease similar to postmortem brain, about 0.5 pH units. Fig. 24 shows the APT images and several conventional MR image types at a time point of 2 h postictus. The pH-weighted images (i.e. the  $\text{MTR}_{\text{asym}}(3.5 \text{ ppm})$  images) were acquired using RF irradiation at offsets of  $\pm 3.5 \text{ ppm}$ . Several affected regions (caudate nucleus, cortex near caudate, cerebellum) are visible in the isotropic diffusion-weighted images, the APT images (i.e. pH-weighted images) and the

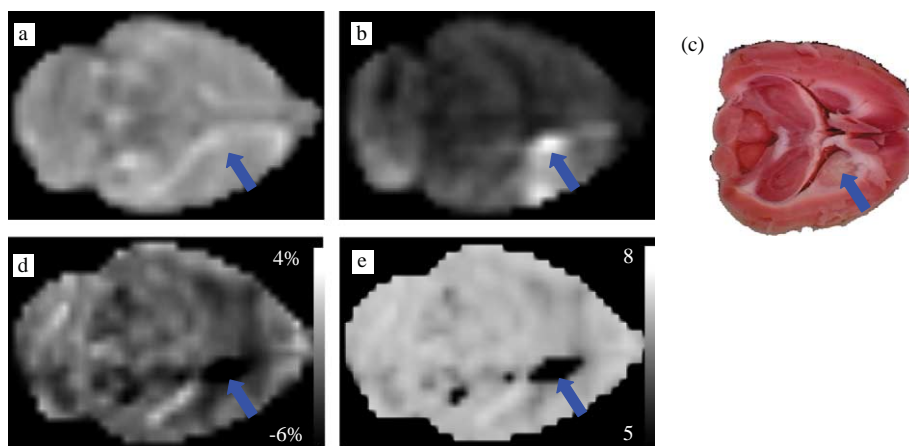


Fig. 24.  $T_2$ -weighted MRI (a), diffusion-weighted MRI (b), TTC (2,3,5-triphenyltetrazolium chloride) stain (c), absolute  $\text{MTR}_{\text{asym}}(3.5 \text{ ppm})$  images (d), and an absolute pH map (e) for ischemic rat brain. MRI data were acquired at 4.7 T. The area of infarction visible on the right side of both the pH-weighted and pH images is located in the caudate nucleus (blue arrow), a region commonly affected by infarction following MCA occlusion, as confirmed by the diffusion-weighted image and by histology. No infarct is visible on the  $T_2$ -weighted image (a). Reprinted from [25], with permission from the authors and Nature Publishing Group.



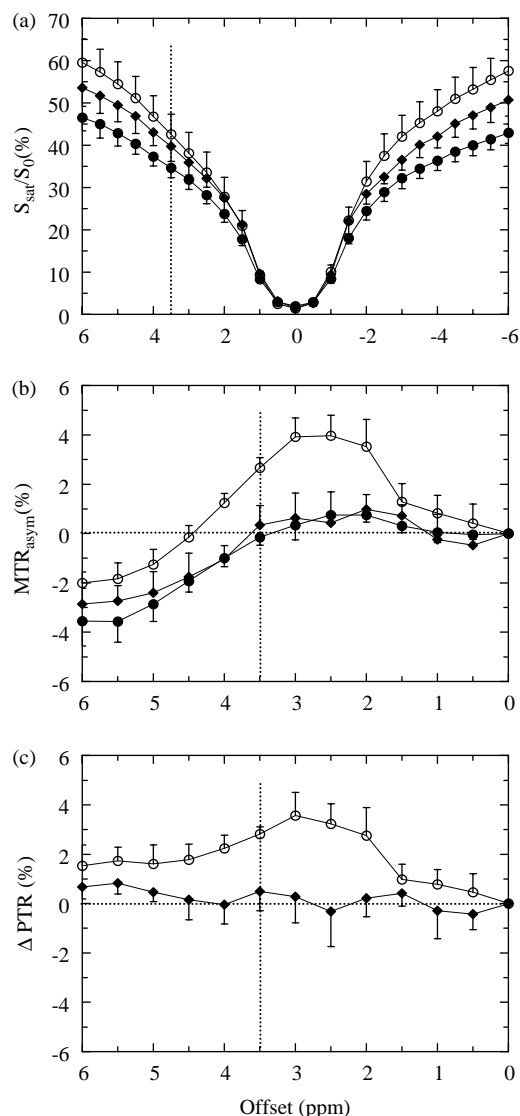


Fig. 25. z-Spectra,  $MTR_{\text{asym}}$  spectra, and  $\Delta PTR$  spectra at 4.7 T for the 9L brain tumor model (tumor age 10 or 11 days;  $n=5$ ). Tumor ( $\circ$ ), peritumoral edema ( $\blacklozenge$ ), and contralateral region ( $\bullet$ ). The  $MTR_{\text{asym}}$  spectrum in tumor is different from those for postmortem normal brain and ischemic brain, and the magnitude of  $\Delta PTR$  is positive at the offset range of 2–5 ppm. Reprinted from [26], with permission from Wiley-Liss, Inc.

calculated pH map, but no effect was visible on the  $T_2$ -weighted images. This indicates good sensitivity of the APT approach for measuring acute pH changes. In a recent conference abstract, Sun et al. [161] reported that the pH effects can be determined before changes in diffusion, which may be important for treatment decisions in clinical acute stroke.

### 6.3. APT imaging of brain tumors

As mentioned above, APT contrast also reflects the tissue content of labile amide protons of mobile proteins and peptides and should thus be able to provide an assessment of endogenous protein/peptide content. This possibility was recently demonstrated in a 9L rat brain tumor model by Zhou

et al. [26]. When acquiring z-spectra (Fig. 25a) for regions localized in the tumor and peritumoral tissue, the investigators found an increase in signal intensity over the complete frequency range compared to regions localized in contralateral brain tissue. However, when studying the  $MTR_{\text{asym}}$  spectra (Fig. 25b), the tumor regions showed an increase in PTR over a range of offsets between 2 and 5 ppm, while the peritumoral regions did not. Interestingly, the maximum change was found to be at offsets between 2 and 3.5 ppm (Fig. 25c). This was attributed to the flexible side chains of proteins, which have a composite amide resonance around 6.8 ppm in the proton spectrum (2 ppm offset from water). It is important to note that the intracellular pH of tumors has been determined to be neutral to slightly alkaline ( $<0.1$  unit), as measured by  $^{31}\text{P}$  MRS using the resonance of inorganic phosphate [136,162–164]. In addition, increased tissue water content and relaxation rates are two possible contributing factors. However, it was concluded that increased protein/peptide content is the most predominant cause of the increased  $MTR_{\text{asym}}$  in the brain tumor, due to the fact that the other contributions are very small. Fig. 26 compares the acquired  $MTR_{\text{asym}}$  (3.5 ppm) or APT-weighted images, with several common MR image types and histology. It is important to note that the APT images show a clear boundary of the tumor, in good qualitative agreement with histology.

Recently, in a conference abstract, Jones et al. [118] reported a first exploratory APT study for brain tumor patients on a 3 T whole body clinical scanner. These preliminary results confirmed an intensity increase in the tumor in the APT-weighted image compared to contralateral normal appearing white matter. Also, in several patients, no APT enhancement was found in edema regions that appeared hyperintense on several conventional MRI images. The fact that such regions did not show Gd-enhancement and were confirmed to be edema supports the potential capability of APT to differentiate the edema from tumor. Future studies using such multi-modal MR exams (including MRI and MRSI) for brain tumor patients will have to show whether APT imaging would be a useful addition to modern brain tumor imaging and perhaps to the imaging of tumors in other body regions.

## 7. Technical considerations

### 7.1. Field strength and homogeneity

As mentioned above, a successful CEST experiment has the prerequisite of selectively irradiating exchangeable solute protons, which basically is equivalent to the requirement of slow or intermediate exchange ( $\Delta\omega_{\text{sw}}\tau_s \geq 1$ ) on the NMR time scale. However, when quantification of CEST effects is the issue, deviations from slow exchange will complicate the situation. Consequently, the availability of high magnetic fields is of great advantage to CEST imaging. At higher field strengths, a disturbing effect such as direct water saturation can be reduced and many functional groups with low to intermediate exchange rates (on the order of  $1000\text{ s}^{-1}$ ) may be useable for CEST experiments. For example, when using



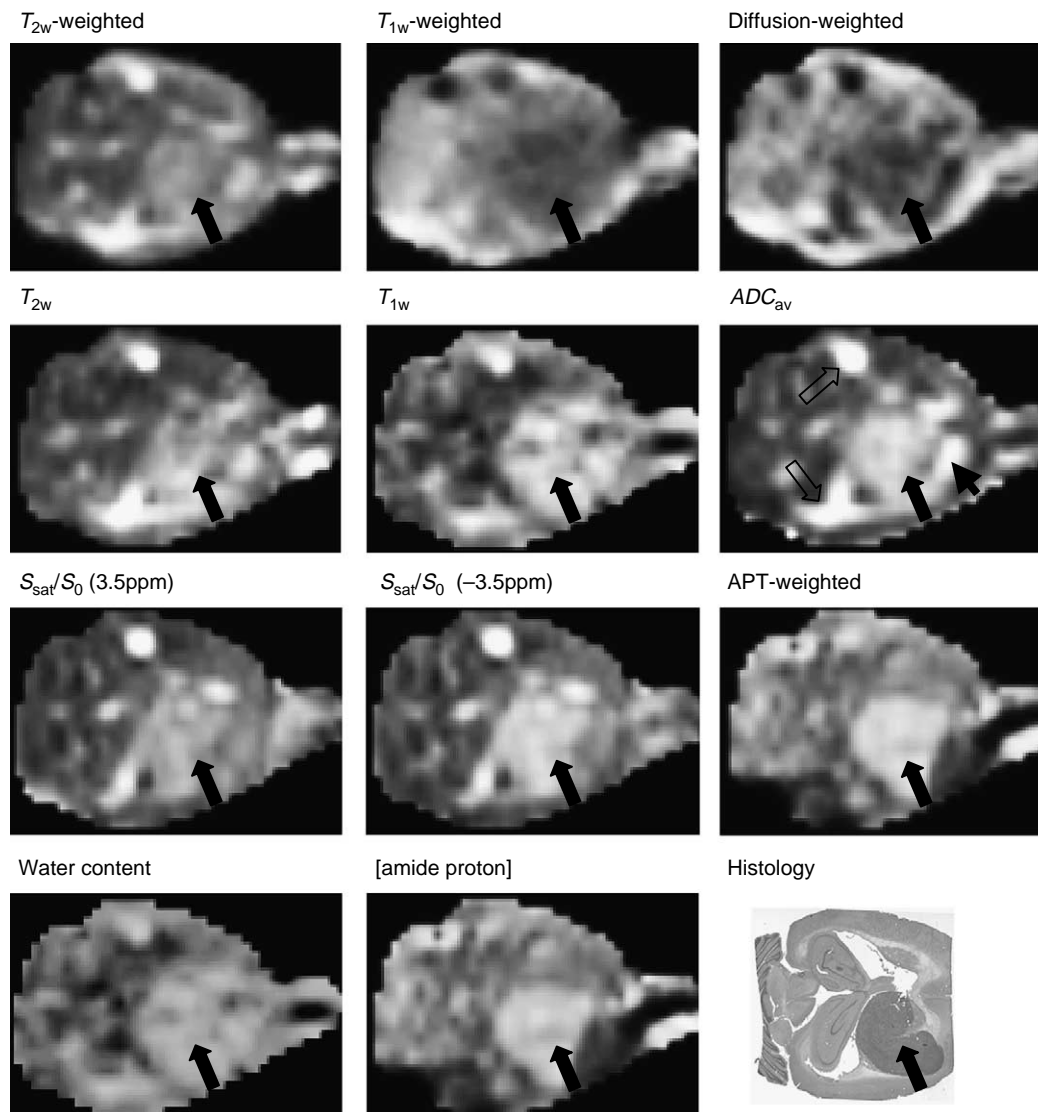


Fig. 26. Comparison of several images at 4.7 T for a 9L glioma (10 or 11 days) in a rat. The glioma (arrow) is visible in all the MR images, as confirmed by histology, but it is much better defined in the APT-weighted image. Arrow head: peritumoral tissue, and open arrow: CSF. The APT-weighted image (16 scans) was acquired using frequency-labeling of offsets at  $\pm 3.5$  ppm from water;  $B_0$  inhomogeneity was corrected using field maps. Reprinted from [26], with permission from Wiley-Liss, Inc.

lower field, the slow-intermediate exchange requirement may break down for the rapidly exchanging poly(rU) imino protons at 10.8 ppm. At 3 T, which is the highest field strength currently available in the clinic, we have  $\Delta\omega_{sw} = 4825$  rad/s, which is on the order of magnitude of the exchange rate at physiological pH and temperature ( $k_{sw} = 5880$  s $^{-1}$  for pH 7.3 and 37 °C [21]). Furthermore, the  $T_1$  of water increases with the field strength, allowing prolonged storage of saturation in the water pool (Eq. (20)). Therefore, APT contrast is expected to increase at higher field.

On the other hand,  $B_0$  field homogeneity is very important for CEST-type experiments, especially for in vivo studies. The potential problem that can arise due to field inhomogeneity is a shift of the z-spectrum with respect to the water zero frequency for the whole volume. For imaging, shimming and RF settings are often based on the NMR signal from a whole volume or tissue (e.g. a head); therefore, the imaging slice or some local

regions of interest may have a somewhat different frequency offset and it is possible that the efficiency of the applied selective RF irradiation is reduced. It is therefore advised to always acquire multiple frequencies in the CEST-type study. If there is time to acquire a complete z-spectrum, the  $B_0$  inhomogeneity can be corrected on a pixel-by-pixel basis using curve fitting [25,26]. When time is more restricted, the  $B_0$  inhomogeneity in the CEST images can be corrected by acquiring a limited number of additional offset images. The shifts between voxels are then corrected using a field map. In their early experiments, Zhou et al. [85] noticed that it is difficult to correct for imaging artifacts in the cerebrospinal fluid (CSF) regions, which sometimes are larger than the small APT effects that are the goal of the study. It should be noticed that these effects are not really due to field inhomogeneities but that they may be associated with the low signal-to-noise ratio in the APT-weighted images for these CSF regions [85].

Obviously, it is the best way to carefully optimize shimming (slice shimming, volume shimming, higher-order shimming, etc.) prior to the experiments, which may reduce some of the need for posthoc correction.

Finally, to guarantee homogeneous saturation on the sample,  $B_1$  field homogeneity is crucial. This can be reasonably well achieved with body coil excitation at 1.5 T, but becomes more difficult at high field due to the limitation in wavelength for the proton frequency with respect to the size of the brain (and body). At the new field strength of 7 T, excitation efficiency is often higher in the center of the brain, which may lead to problems with CEST imaging.

### 7.2. Saturation scheme

Fig. 27 shows the typical CEST-type imaging sequence, in which the RF saturation scheme (label and transfer) can be either continuous wave (CW) or pulsed. Although a CEST sequence is in form similar to the traditional MT sequences available on all clinical scanners, some small adjustments have to be performed to optimize the sequence. The reason is that the commercially available MT schemes were designed to detect large MT effects from irradiated protons associated with immobile macromolecules and membranes at offsets of 10–100 kHz. As CEST contrast agents have a smaller proton content, it is important the saturation transfer scheme must be optimized according to the proper theoretical model to maximize the effects. In addition, except in some PARACEST experiments, CEST effects take place in a small offset range around the water resonance frequency and, when RF saturation power is too strong, may be reduced significantly or eliminated by the effect of direct water saturation. Therefore, a very weak and selective RF field should be applied to the exchangeable solute proton pool to avoid too much direct water signal intensity attenuation. Finally, the CEST effect is acquired by subtracting MT spectra obtained at the positive offset from

those at the corresponding negative offset with respect to water. This requires a longer total experimental time. Large CEST effect, low saturation power, short saturation time, and short TR will be several criteria of an optimized CEST imaging and spectroscopy pulse sequence. These issues obviously become more critical for clinical studies. In particular, and similar to MT imaging, RF power deposition is a major concern. Unfortunately, power deposition increases with the square of the magnetic field strength.

### 7.3. Interference from lipid signals

To obtain APT images at reasonable spatial and temporal resolution in vivo, the RF saturation scheme can be combined with fast imaging methods such as fast spin echo (FSE) or echo planar imaging (EPI). When performing such APT–EPI imaging during stroke studies in animals, Sun et al. [165] noticed that a small EPI fat artifact did not subtract out from the images in the asymmetry analysis. Fig. 28 shows characteristic images acquired one hour after MCAO preparation. A fat artifact is clearly visible in the left APT image without fat suppression. The single-shot EPI acquisition had an acquisition time of 20 ms and an effective bandwidth of only 3200 Hz along the phase encoding axis. At 4.7 T, the chemical shift difference between water and lipid leads to a shift of 14 pixels down the phase encoding axis, folding the fat signal into the brain where it overlaps with the stroke lesion. Interestingly, APT images are particularly prone to this artifact because the chemical shift difference between water and the lipid protons at 1.3 ppm is the same as that between water and the amide protons at 8.3 ppm, but of opposite sign. When acquiring the APT reference image at  $-3.5$  ppm (1.3 ppm in the proton spectrum), the lipid signal is suppressed. However, there is no

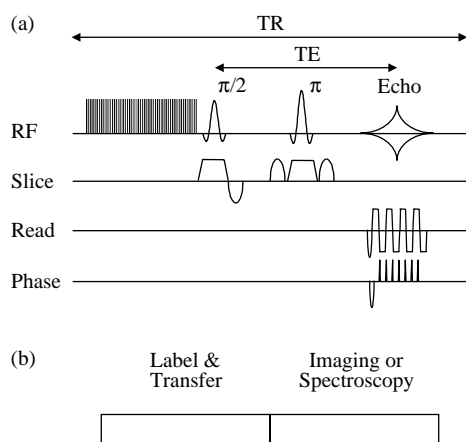


Fig. 27. CEST imaging and spectroscopy pulse sequences. (a) 2D imaging using spin echo EPI acquisition and pulse train saturation scheme. (b) A general pulse sequence scheme. Off-resonance saturation schemes can be either pulse train or continuous wave. Data acquisition can be imaging (2D, multislice or 3D) or spectroscopy models. Modified from [85], with permission from Wiley-Liss, Inc.

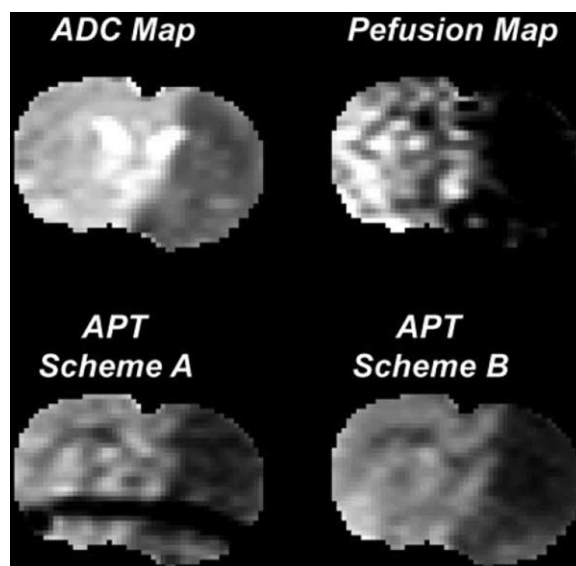


Fig. 28. MRI images at 4.7 T of rat brain acquired at 1 h after MCA occlusion. An EPI fat artifact appears as a dark stripe in the APT image based on a spin echo imaging sequence without fat suppression (Scheme A) and is substantially suppressed by the use of a chemical shift-selective refocusing pulse (Scheme B). Reprinted from [165], with permission from Wiley-Liss, Inc.

lipid suppression when saturating the amide protons at +3.5 ppm and asymmetry analysis will not remove the fat artifact.

In order to obtain an appropriate APT image, the lipid resonance has to be suppressed equally at both offsets. As shown on the right side in Fig. 28, Sun et al. [165] demonstrated that this can be achieved by using a spin echo imaging sequence with a water-selective refocusing pulse [119,166]. The results showed a suppression of 93% of the lipid artifact. The chemical shift selective pulse used was a 4 ms Gaussian pulse, corresponding to a bandwidth of about 445 Hz at 1% of the signal intensity. When shimming a rat brain over the whole slice, the typical line width at the 10% of the intensity of the water line is of the order of 60–100 Hz. Thus, at 4.7 T (1 ppm = 200 Hz), the chemical shift selective pulse was sufficiently broad for refocusing most of the water resonance while only minimally affecting the lipid protons. The approach should be useful for all CEST agents that have exchangeable protons in the spectral range of amide protons.

## 8. Conclusions

The CEST mechanism has opened a completely new avenue of MRI research. Even though the principles were first realized in 1990, it took until about the year 2000 before a pioneering paper by Balaban's group opened up this field. CEST technology allows several new types of applications and the results shown in this early review are probably only the tip of the iceberg. Multiple CEST-type applications are currently being evaluated, including pH imaging, metabolite detection, imaging of cellular mobile proteins and peptides, CEST reporter genes, etc. Future work will have to realize their potential in the clinical setting.

## Acknowledgements

This work was supported in part by grants from NIH (EB02634, EB02666, EB05252, and RR15241) and the Whitaker Foundation.

## References

- [1] U. Liddel, N.F. Ramsey, *J. Chem. Phys.* 19 (1951) 1608.
- [2] J.T. Arnold, M.E. Packard, *J. Chem. Phys.* 19 (1951) 1608–1609.
- [3] H.S. Gutowsky, A. Saika, *J. Chem. Phys.* 21 (1953) 1688–1694.
- [4] H.S. Gutowsky, C.H. Holm, *J. Chem. Phys.* 25 (1956) 1228–1234.
- [5] D.L. Arnold, *Phys. Rev. Lett.* 102 (1956) 136–150.
- [6] H.M. McConnell, *J. Chem. Phys.* 28 (1958) 430–431.
- [7] D.E. Woessner, *J. Chem. Phys.* 35 (1961) 41–48.
- [8] S. Forsen, R.A. Hoffman, *J. Chem. Phys.* 39 (1963) 2892–2901.
- [9] A. Allerhand, H.S. Gutowsky, *J. Chem. Phys.* 41 (1964) 2115–2126.
- [10] H.S. Gutowsky, R.L. Vold, E.J. Wells, *J. Chem. Phys.* 43 (1965) 4107–4125.
- [11] J. Jeener, Ampere Summer School, Basko Polje, Yugoslavia, 1971.
- [12] W.P. Aue, E. Bartholdi, R.R. Ernst, *J. Chem. Phys.* 64 (1976) 2229–2246.
- [13] J. Jeener, B.H. Meier, P. Bachmann, R.R. Ernst, *J. Chem. Phys.* 71 (1979) 4546–4553.
- [14] R.R. Ernst, G. Bodenhausen, A. Wokaun, *Principles of Nuclear Magnetic Resonance in One and Two Dimensions*, Clarendon Press, Oxford, 2003.
- [15] R.S. Balaban, H.L. Kantor, J.A. Ferretti, *J. Biol. Chem.* 258 (1983) 2787–2789.
- [16] R.S. Balaban, J.A. Ferretti, *Proc. Natl Acad. Sci. USA* 80 (1983) 1241–1245.
- [17] S.D. Wolff, R.S. Balaban, *J. Magn. Reson.* 86 (1990) 164–169.
- [18] V. Guivel-Scharen, T. Sinnwell, S.D. Wolff, R.S. Balaban, *J. Magn. Reson.* 133 (1998) 36–45.
- [19] K.M. Ward, A.H. Aletras, R.S. Balaban, *J. Magn. Reson.* 143 (2000) 79–87.
- [20] N. Goffeney, J.W.M. Bulte, J. Duyn, L.H. Bryant, P.C.M. van Zijl, *J. Am. Chem. Soc.* 123 (2001) 8628–8629.
- [21] K. Snoussi, J.W.M. Bulte, M. Gueron, P.C.M. van Zijl, *Magn. Reson. Med.* 49 (2003) 998–1005.
- [22] S. Zhang, P. Winter, K. Wu, A.D. Sherry, *J. Am. Chem. Soc.* 123 (2001) 1517–1578.
- [23] S. Zhang, A.D. Sherry, *J. Solid State Chem.* 171 (2003) 38–43.
- [24] S. Aime, A. Barge, D. Delli Castelli, F. Fedeli, A. Mortillaro, F.U. Nielsen, E. Terreno, *Magn. Reson. Med.* 47 (2002) 639–648.
- [25] J. Zhou, J. Payen, D.A. Wilson, R.J. Traystman, P.C.M. van Zijl, *Nat. Med.* 9 (2003) 1085–1090.
- [26] J. Zhou, B. Lal, D.A. Wilson, J. Laterra, P.C.M. van Zijl, *Magn. Reson. Med.* 50 (2003) 1120–1126.
- [27] C.S. Johnson, *Adv. Magn. Reson.* 1 (1965) 33–102.
- [28] R. Willem, *Progr. NMR Spectr.* 20 (1987) 1–94.
- [29] H. Desvaux, P. Berthault, *Progr. NMR Spectr.* 35 (1999) 295–340.
- [30] C.E. Dempsey, *Progr. NMR Spectr.* 39 (2001) 135–170.
- [31] A.D. Bain, *Progr. NMR Spectr.* 43 (2003) 63–103.
- [32] J.R. Alger, R.G. Shulman, *Q. Rev. Biophys.* 17 (1984) 83–124.
- [33] P.G. Morris, *Annu. Rep. NMR Spectr.* 20 (1988) 1–60.
- [34] D. Leibfritz, W. Dreher, *NMR Biomed.* 14 (2001) 65–76.
- [35] L.M. Jackman, F.A. Cotton, *Dynamic Nuclear Magnetic Resonance Spectroscopy*, Academic Press, New York, 1975.
- [36] J.I. Kaplan, G. Fraenkel, *NMR of Chemically Exchanging Systems*, Academic Press, New York, 1980.
- [37] J. Sandstrom, *Dynamic NMR Spectroscopy*, Academic Press, London, 1982.
- [38] J. Cavanagh, W.J. Fairbrother, A.G. Palmer III, N.J. Skelton, *Protein NMR Spectroscopy: Principles and Practice*, Academic Press, San Diego, CA, 1996.
- [39] F.W. Dahlquist, K.J. Longmuir, R.B. Du Vernet, *J. Magn. Reson.* 17 (1975) 406–410.
- [40] T.R. Brown, S. Ogawa, *Proc. Natl Acad. Sci. USA* 74 (1977) 3627–3631.
- [41] T.R. Brown, K. Ugurbil, R.G. Shulman, *Proc. Natl Acad. Sci. USA* 74 (1977) 5551–5553.
- [42] J.R. Alger, J.H. Prestegard, *J. Magn. Reson.* 27 (1977) 137–141.
- [43] I.D. Campbell, C.M. Dobson, R.G. Ratcliffe, *J. Magn. Reson.* 27 (1977) 455–463.
- [44] K. Ugurbil, *J. Magn. Reson.* 64 (1985) 207–219.
- [45] R.G.S. Spencer, J.A. Balschi, J.S. Leigh, J.S. Ingwall, *Biophys. J.* 54 (1988) 921–929.
- [46] P.A. Bottomley, C.J. Hardy, *J. Magn. Reson.* 99 (1992) 443–448.
- [47] H. Lei, K. Ugurbil, W. Chen, *Proc. Natl Acad. Sci. USA* 100 (2003) 14409–14414.
- [48] S.A. Gabel, T.M. O'Connell, E. Murphy, R.E. London, *Am. J. Physiol.* (1997) C1415–C1419.
- [49] J.X. Yu, V.D. Kodibagkar, W. Cui, R.P. Mason, *Curr. Med. Chem.* 12 (2005) 819–848.
- [50] N.M. Szeverenyi, M.J. Sullivan, G.E. Macial, *J. Magn. Reson.* 47 (1982) 462–475.
- [51] J. Shen, *Magn. Reson. Med.* 54 (2005) 1321–1326.
- [52] H.T. Edzes, E.T. Samulski, *Nature* 265 (1977) 521–523.
- [53] H.T. Edzes, E.T. Samulski, *J. Magn. Reson.* 31 (1978) 207–229.
- [54] D.F. Gochberg, R.P. Kennan, J.C. Gore, *Magn. Reson. Med.* 38 (1997) 224–231.

- [55] D.F. Gochberg, J.C. Gore, *Magn. Reson. Med.* 49 (2003) 501–505.
- [56] O.H.J. Grohn, J.A. Lukkariinen, M.J. Silvennoinen, A. Pitkanen, P.C.M. van Zijl, R.A. Kauppinen, *Magn. Reson. Med.* 42 (1999) 268–276.
- [57] O.H.J. Grohn, M.I. Kettunen, H.I. Makela, M. Penttonen, A. Pitkanen, J.A. Lukkariinen, R.A. Kauppinen, *J. Cereb. Blood Flow Metab.* 20 (2000) 1457–1466.
- [58] H.I. Makela, O.H.J. Grohn, M.I. Kettunen, R. Kauppinen, *Biochem. Biophys. Res. Commun.* 289 (2001) 813–818.
- [59] M.J. Silvennoinen, M.I. Kettunen, C.S. Clingman, R. Kauppinen, *Arch. Biochem. Biophys.* 405 (2002) 78–86.
- [60] D. Idiyatullin, S. Michaeli, M. Garwood, *J. Magn. Reson.* 171 (2004) 330–337.
- [61] S. Michaeli, D.J. Sorce, D. Idiyatullin, K. Ugurbil, M. Garwood, *J. Magn. Reson.* 169 (2004) 293–299.
- [62] S. Michaeli, H. Grohn, O. Grohn, D.J. Sorce, R. Kauppinen, C.S. Springer, K. Ugurbil, M. Garwood, *Magn. Reson. Med.* 53 (2005) 823–829.
- [63] A. Vinogradov, S. Zhang, A. Lubag, J.A. Balschi, A.D. Sherry, R.E. Lenkinski, *J. Magn. Reson.* 176 (2005) 54–63.
- [64] S. Zhang, M. Merritt, D.E. Woessner, R. Lenkinski, A.D. Sherry, *Acc. Chem. Res.* 36 (2003) 783–790.
- [65] J. Zhou, P.C.M. van Zijl, Internal Workshop: Biomedical Magnetic Resonance, New Delhi, India, 2005, pp. 353–361.
- [66] S.D. Wolff, R.S. Balaban, *Magn. Reson. Med.* 10 (1989) 135–144.
- [67] R.S. Balaban, T.L. Ceckler, *Magn. Reson. Q.* 8 (1992) 116–137.
- [68] R.G. Bryant, *Annu. Rev. Biophys. Biomol. Struct.* 25 (1996) 29–53.
- [69] R.M. Henkelman, G.J. Stanisz, S.J. Graham, *NMR Biomed.* 14 (2001) 57–64.
- [70] B.P. Hills, *Mol. Phys.* 76 (1992) 489–508.
- [71] B.P. Hills, *Mol. Phys.* 76 (1992) 509–523.
- [72] E. Liepinsh, G. Otting, *Magn. Reson. Med.* 35 (1996) 30–42.
- [73] R.P. Kennan, K.A. Richardson, J. Zhong, M.J. Maryanski, J.C. Gore, *J. Magn. Reson. B* 110 (1996) 267–277.
- [74] D.F. Gochberg, R.P. Kennan, M.J. Maryanski, J.C. Gore, *J. Magn. Reson.* 131 (1998) 191–198.
- [75] P.C.M. van Zijl, J. Zhou, N. Mori, J. Payen, S. Mori, *Magn. Reson. Med.* 49 (2003) 440–449.
- [76] M.T. McMahon, A.A. Gilad, J. Zhou, P.Z. Sun, J.W.M. Bulte, P.C.M. van Zijl, *Magn. Reson. Med.* (In press).
- [77] A.P. Dagher, A. Aletras, P. Choyke, R.S. Balaban, *J. Magn. Reson. Imaging* 12 (2000) 745–748.
- [78] S. Aime, D. Delli Castelli, E. Terreno, *J. Am. Chem. Soc.* 124 (2002) 9364–9365.
- [79] S. Zhang, R. Trokowski, A.D. Sherry, *J. Am. Chem. Soc.* 125 (2003) 15288–15289.
- [80] K.M. Ward, R.S. Balaban, *Magn. Reson. Med.* 44 (2000) 799–802.
- [81] P.C.M. van Zijl, N. Goffeney, J.H. Duyn, L.H. Bryant, J.W.M. Bulte, Proceedings of the ninth Annual Meeting ISMRM, Glasgow, 2001, p. 878.
- [82] S. Aime, D. Delli Castelli, *Angew. Chem. Int. Ed. Engl.* 41 (2002) 4334–4336.
- [83] E. Terreno, D.D. Castelli, G. Cravotto, L. Milone, S. Aime, *Invest. Radiol.* 39 (2004) 235–243.
- [84] A.A. Gilad, M.T. McMahon, P.T. Winnard Jr., V. Raman, J.W. Bulte, P.C.M. van Zijl, Proceedings of the 13th Annual Meeting ISMRM, Miami, 2005, p. 363.
- [85] J. Zhou, D.A. Wilson, P.Z. Sun, J.A. Klaus, P.C.M. van Zijl, *Magn. Reson. Med.* 51 (2004) 945–952.
- [86] D.E. Woessner, S. Zhang, M.E. Merritt, A.D. Sherry, *Magn. Reson. Med.* 53 (2005) 790–799.
- [87] R.M. Henkelman, X. Huang, Q.-S. Xiang, G.J. Stanisz, S.D. Swanson, M.J. Bronskill, *Magn. Reson. Med.* 1993(1993) 759–766.
- [88] X. Wu, J.J. Listinsky, *J. Magn. Reson. B* 105 (1994) 73–76.
- [89] E. Baguet, C. Roby, *J. Magn. Reson. A* 108 (1994) 189–195.
- [90] E. Baguet, C. Roby, *J. Magn. Reson.* 128 (1997) 149–160.
- [91] P.Z. Sun, P.C.M. van Zijl, J. Zhou, *J. Magn. Reson.* 175 (2005) 193–200.
- [92] P.B. Kingsley, W.G. Monahan, *J. Magn. Reson.* 143 (2000) 360–375.
- [93] P.B. Kingsley, W.G. Monahan, *Magn. Reson. Med.* 43 (2000) 810–819.
- [94] R.G.S. Spencer, A. Horska, J.A. Ferretti, G.H. Weiss, *J. Magn. Reson. B* 101 (1993) 294–296.
- [95] A. Horska, R.G.S. Spencer, *MAGMA* 5 (1997) 159–163.
- [96] S. Ogawa, T.M. Lee, A.R. Kay, D.W. Tank, *Proc. Natl. Acad. Sci. USA* 87 (1990) 9868–9872.
- [97] J.W. Belliveau, D.N. Kennedy Jr., R.C. McKinstry, B.R. Buchbinder, R.M. Weisskoff, M.S. Cohen, J.M. Vevea, T.J. Brady, B.R. Rosen, *Science* 254 (1991) 716–719.
- [98] P.C.M. van Zijl, S.M. Eleff, J.A. Ulatowski, J.M.E. Oja, A.M. Ulug, R.J. Traystman, R.A. Kauppinen, *Nat. Med.* 4 (1998) 159–167.
- [99] J. Zhou, J. Payen, P.C.M. van Zijl, *Magn. Reson. Med.* 53 (2005) 356–366.
- [100] J. Pekar, P. Jezzard, D.A. Roberts, J.S. Leigh, J.A. Frank, A.C. McLaughlin, *Magn. Reson. Med.* 35 (1996) 70–79.
- [101] S.D. Swanson, Y. Pang, Proceedings of the 11th Annual Meeting ISMRM, Toronto, 2003, p. 660.
- [102] J. Hua, C.K. Jones, P.C.M. van Zijl, J. Zhou, Proceedings of the 13th Annual Meeting ISMRM, Miami, 2005, p. 416.
- [103] S.W. Englander, N.W. Downer, H. Teitelbaum, *Annu. Rev. Biochem.* 41 (1972) 903–924.
- [104] K. Wuthrich, G. Wagner, *J. Mol. Biol.* 130 (1979) 1–18.
- [105] K. Wuthrich, *NMR of Proteins and Nucleic Acids*, Wiley, New York, NY, 1986.
- [106] K.L. Behar, T. Ogino, *Magn. Reson. Med.* 17 (1991) 285–303.
- [107] K.L. Behar, T. Ogino, *Magn. Reson. Med.* 30 (1993) 38–44.
- [108] K.L. Behar, D.L. Rothman, D.D. Spencer, Q.A.C. Petroff, *Magn. Reson. Med.* 32 (1994) 294–302.
- [109] R.A. Kauppinen, H. Kokko, S.R. Williams, *J. Neurochem.* 58 (1992) 967–974.
- [110] R.A. Kauppinen, J. Palvimo, *Magn. Reson. Med.* 25 (1992) 398–407.
- [111] R.A. Kauppinen, T. Nissinen, J. Hakumaki, S.R. Williams, *NMR Biomed.* 6 (1993) 242–247.
- [112] G.D. Graham, *Neurosci. Res.* 2 (1996) 309–312.
- [113] J. Pfeuffer, I. Tkac, S.W. Provencher, R. Gruetter, *J. Magn. Reson.* 141 (1999) 104–120.
- [114] C. Gasparovic, G.A. Rosenberg, J.A. Wallace, E.Y. Estrada, K. Roberts, A. Pastuszyn, W. Ahmed, G.D. Graham, *Neurosci. Lett.* 301 (2001) 87–90.
- [115] I. Mader, U. Seeger, R. Weissert, U. Klose, T. Naegle, A. Melms, W. Grodd, *Brain* 124 (2001) 953–961.
- [116] S. Mori, S.M. Eleff, U. Pilatus, N. Mori, P.C.M. van Zijl, *Magn. Reson. Med.* 40 (1998) 36–42.
- [117] W. Chen, J. Hu, *J. Magn. Reson.* 140 (1999) 363–370.
- [118] C.K. Jones, M.J. Schlosser, P.C.M. van Zijl, M.G. Pomper, X. Golay, J. Zhou, Proceedings of the 13th Annual Meeting ISMRM, Miami, 2005, p. 1256.
- [119] S. Mori, C. Abeygunawardana, P.C.M. van Zijl, J.M. Berg, *J. Magn. Reson. B* 110 (1996) 96–101.
- [120] S. Mori, C. Abeygunawardana, J.M. Berg, P.C.M. van Zijl, *J. Am. Chem. Soc.* 119 (1997) 6844–6852.
- [121] A.K. Covington, R.A. Robinson, R.G. Bates, *J. Phys. Chem.* 70 (1966) 3820–3824.
- [122] R.B. Lauffer, *Chem. Rev.* 87 (1987) 901–927.
- [123] P. Caravan, J.J. Ellison, T.J. McMurray, R.B. Lauffer, *Chem. Rev.* 99 (1999) 2293–2352.
- [124] A.E. Merbach, E. Toth, *The Chemistry of Contrast Agents in Medical Magnetic Resonance Imaging*, Wiley, Chichester, 2001.
- [125] S. Aime, M. Botta, M. Fasano, E. Terreno, *Acc. Chem. Res.* 32 (1999) 941–949.
- [126] S. Aime, C. Cabella, S. Colombatto, S. Geninatti Crich, E. Gianolio, F. Maggioni, *J. Magn. Reson. Imaging* 16 (2002) 394–406.
- [127] S. Aime, M. Botta, E. Terreno, *Adv. Inorg. Chem.* 57 (2005) 173–237.
- [128] M.P. Lowe, *Aust. J. Chem.* 55 (2002) 551–556.
- [129] M.P. Lowe, *Curr. Pharm. Biotechnol.* 5 (2004) 519–528.
- [130] S. Aime, A. Barge, M. Botta, A.S. De Sousa, D. Parker, *Angew. Chem. Int. Ed. Engl.* 37 (1998) 2673–2675.

- [131] S. Zhang, K. Wu, M.C. Biewer, A.D. Sherry, *Inorg. Chem.* 40 (2001) 4284–4290.
- [132] L.D. Shrode, H. Tapper, S. Grinstein, *J. Bioenerg. Biomembr.* 29 (1997) 393–399.
- [133] P.A. Bottomley, B.P. Drayer, L.S. Smith, *Radiology* 160 (1986) 763–766.
- [134] S.R. Levine, J.A. Helpert, K.M.A. Welch, A.M.Q. Vandelinde, K.L. Sawaya, E.E. Brown, N.M. Ramadan, R.K. Deveshwar, R.J. Ordidge, *Radiology* 185 (1992) 537–544.
- [135] D.B. Kintner, M.E. Anderson, K.A. Sailor, G. Dienel, J.H. Fitzpatrick Jr., D.D. Gilboe, *J. Neurochem.* 72 (1999) 405–412.
- [136] J.R. Griffiths, *Br J. Cancer* 64 (1991) 425–427.
- [137] R.J. Gillies, Z. Bhujwalla, J. Evelhoch, M. Garwood, M. Neeman, S.P. Robinson, C.H. Sotak, B. van der Sanden, *Neoplasia* 2 (2000) 139–151.
- [138] J.L. Evelhoch, R.J. Gillies, G.S. Karczmar, J.A. Koutcher, R.J. Maxwell, O. Nalcioğlu, N. Raghunand, S.M. Ronen, B.D. Ross, H.M. Swartz, *Neoplasia* 2 (2000) 152–165.
- [139] Z. Bhujwalla, D. Artemov, M. Solaiyappan, *Exper. Oncology* 22 (2000) 3–7.
- [140] R.J. Gillies, N. Raghunand, M. Garcia-Martin, R.A. Gatenby, *IEEE Eng. Med. Biol. Mag.* (2004) 57–64.
- [141] R. Zhou, N. Bansal, D.B. Leeper, J.D. Glickson, *Cancer Res.* 60 (2000) 3532–3536.
- [142] R. Zhou, N. Bansal, D.B. Leeper, S. Pickup, J.D. Glickson, *Acad. Radiol.* 8 (2001) 571–582.
- [143] R.B. Moon, J.H. Richards, *J. Biol. Chem.* 248 (1973) 7276–7278.
- [144] O.A.C. Petroff, J.W. Prichard, K.L. Behar, J.R. Alger, J.A. Denhoff, R.G. Shulman, *Neurology* 35 (1985) 781–788.
- [145] R.J. Gillies, Z. Liu, Z. Bhujwalla, *Am. J. Physiol.* 267 (1994) C195–C203.
- [146] G.E. Soto, Z. Zhu, J.L. Evelhoch, J.J.H. Ackerman, *Magn. Reson. Med.* 36 (1996) 698–704.
- [147] S. Gil, P. Zaderenzo, F. Cruz, S. Cerdan, P. Ballesteros, *Bioorg. Med. Chem.* 2 (1994) 305–314.
- [148] R. van Sluis, Z.M. Bhujwalla, N. Raghunand, P. Ballesteros, J. Alvarez, S. Cerdan, J. Galons, R.J. Gillies, *Magn. Reson. Med.* 41 (1999) 743–750.
- [149] Z. Bhujwalla, D. Artemov, P. Ballesteros, S. Cerdan, R.J. Gillies, M. Solaiyappan, *NMR Biomed.* 15 (2002) 114–119.
- [150] M. Garcia-Martin, G. Herigault, C. Remy, R. Farion, P. Ballesteros, J.A. Coles, S. Cerdan, A. Ziegler, *Cancer Res.* 61 (2001) 6524–6531.
- [151] P. Vermathen, A.A. Capizzano, A.A. Maudsley, *Magn. Reson. Med.* 43 (2000) 665–675.
- [152] J.A. Helpert, J.C. Curtis, D. Hearshen, M.B. Smith, K.M.A. Welch, *Magn. Reson. Med.* 5 (1987) 302–305.
- [153] N. Raghunand, C. Howison, A.D. Sherry, S.R. Zhang, R.J. Gillies, *Magn. Reson. Med.* 49 (2003) 249–257.
- [154] A.Y. Louie, M.M. Huber, E.T. Ahrens, U. Rothbacher, R. Moats, R.E. Jacobs, S.E. Fraser, T.J. Meade, *Nat. Biotechnol.* 18 (2000) 321–325.
- [155] R. Weissleder, A. Moore, U. Mahmood, R. Bhorade, H. NBenveniste, E.A. Chiocca, J.P. Basilion, *Nat. Med.* 6 (2000) 351–354.
- [156] S. Aime, D. Delli Castelli, E. Terreno, *Angew. Chem. Int. Ed. Engl.* 42 (2003) 4527–4529.
- [157] S. Aime, D. Delli Castelli, E. Terreno, *Angew. Chem. Int. Ed. Engl.* 44 (2005) 5513–5515.
- [158] S. Zhang, L. Michaudet, S. Burgess, A.D. Sherry, *Angew. Chem. Int. Ed. Engl.* 41 (2002) 1919–1921.
- [159] S. Aime, C. Carrera, D. Delli Castelli, S. Geninatti Crich, E. Terreno, *Angew. Chem. Int. Ed. Engl.* 44 (2005) 1813–1815.
- [160] S. Zhang, A.D. Sherry, C.R. Malloy, *Proceedings of the 13th Annual Meeting ISMRM, Miami, 2005*, p. 2707.
- [161] P. Sun, J. Zhou, W. Sun, J. Huang, P.C.M. van Zijl, *Proceedings of the 13th Annual Meeting ISMRM, Miami, 2005*, p. 984.
- [162] B.D. Ross, R.J. Higgins, J.E. Boggan, B. Knittel, M. Garwood, *Magn. Reson. Med.* 6 (1988) 403–417.
- [163] Y.C. Hwang, S.-G. Kim, J.L. Evelhoch, J.J.H. Ackerman, *Cancer Res.* 52 (1992) 1259–1266.
- [164] D. Maintz, W. Heindel, H. Kugel, R. Jaeger, K.J. Lackner, *NMR Biomed.* 15 (2002) 18–27.
- [165] P. Sun, J. Zhou, W. Sun, J. Huang, P.C.M. van Zijl, *Magn. Reson. Med.* 54 (2005) 222–225.
- [166] D.C. Shungu, J.D. Glickson, *Magn. Reson. Med.* 32 (1994) 277–284.